Actin cables and comet tails organize mitochondrial networks in mitosis

https://doi.org/10.1038/s41586-021-03309-5

Received: 21 May 2020

Accepted: 29 January 2021

Andrew S. Moore[1,2,3], Stephen M. Coscia[1,2,4], Cory L. Simpson[1,2,5], Fabian E. Ortega[6], Eric C. Wait[3], John M. Heddleston[3], Jeffrey J. Nirschl[1,2], Christopher J. Obara[3], Pedro Guedes-Dias[1,2,7], C. Alexander Boecker[1], Teng-Leong Chew[3], Julie A. Theriot[8,9], Jennifer Lippincott-Schwartz[3] & Erika L. F. Holzbaur[1,2,4] ✉

Symmetric cell division requires the even partitioning of genetic information and cytoplasmic contents between daughter cells. Whereas the mechanisms coordinating the segregation of the genome are well known, the processes that ensure organelle segregation between daughter cells remain less well understood[1]. Here we identify multiple actin assemblies with distinct but complementary roles in mitochondrial organization and inheritance in mitosis. First, we find a dense meshwork of subcortical actin cables assembled throughout the mitotic cytoplasm. This network scaffolds the endoplasmic reticulum and organizes three-dimensional mitochondrial positioning to ensure the equal segregation of mitochondrial mass at cytokinesis. Second, we identify a dynamic wave of actin filaments reversibly assembling on the surface of mitochondria during mitosis. Mitochondria sampled by this wave are enveloped within actin clouds that can spontaneously break symmetry to form elongated comet tails. Mitochondrial comet tails promote randomly directed bursts of movement that shuffle mitochondrial position within the mother cell to randomize inheritance of healthy and damaged mitochondria between daughter cells. Thus, parallel mechanisms mediated by the actin cytoskeleton ensure both equal and random inheritance of mitochondria in symmetrically dividing cells.

Mitochondria form morphologically complex networks that rapidly fragment upon mitotic entry[2,3], decouple from microtubules[4] and redistribute throughout the cytoplasm surrounding the mitotic spindle, as seen in cell lines and organotypic cultures (Extended Data Fig. 1a–f). The cytoskeleton is a critical regulator of organelle positioning, so we reasoned that actin filaments may take over as the dominant mitochondrial scaffold following mitochondrial release from microtubules at the start of mitosis. Actin filaments drive mitochondrial segregation in budding yeast[5,6], but whether comparable actin-based mechanisms exist in dividing animal cells remains controversial[4,7], in part owing to the challenge of visualizing sparse subcortical actin assemblies underlying the dense, actin-rich mitotic cortex[8,9] (Extended Data Fig. 2a).

Using high-sensitivity Airyscan microscopy, we resolved a 3D network of actin cables radiating throughout the metaphase cytoplasm (Fig. 1a, Extended Data Fig. 2b–e). The cables were differentially oriented, forming a lattice-like mesh with a pore radius of 320 ± 160 nm (mean ± s.d.) and average maximum circle fitting area of $1.3 \pm 0.2\ \mu\mathrm{m}^2$ (Extended Data Fig. 2f–k). Using grazing-incidence structured illumination microscopy (GI-SIM), we estimated cable widths of 119 ± 18 nm, close to or below the diffraction limit (Extended Data Fig. 2i). Actin cables were excluded from the spindle zone, but crisscrossed the organelle-rich cytoplasm, increasing in density in anaphase (Extended Data Fig. 2l, m).

We observed close associations between mitochondria and actin cables. Individual mitochondria were positioned within pores of the meshwork, co-orienting with neighbouring cables, an alignment observed in all cell lines examined (Fig. 1b, c, Extended Data Fig. 2n–q). Directed translocation of mitochondria along cables was not observed; instead, the movement of both mitochondria and cables appeared diffusive, with transient periods of locally correlated motility (Fig. 1d, Extended Data Fig. 2r–w, Supplementary Video 1). The alignment and co-motility of mitochondria with neighbouring cables suggest that brief and reversible tethering events may loosely couple mitochondria to the meshwork.

Elimination of the meshwork with latrunculin A (LatA) (1 μM for 1 h) or cytochalasin D (CytoD) (100 nM for 1 h) resulted in mitochondrial aggregation, reduced mitochondrial motility, and global mitochondrial positioning defects within the cytoplasm (Fig. 1e, f, Extended Data Fig. 3a–k). To quantify these defects, we labelled cells with the double-stranded DNA (dsDNA) dye PicoGreen, which enabled us to localize individual mitochondrial DNA (mtDNA) nucleoids, even in regions of highly aggregated mitochondrial membranes. Compared with the uniform angular positioning of nucleoids observed in control cells, nucleoids in CytoD- or LatA-treated cells displayed severe angular distribution defects around the spindle. (Fig. 1g–j, Extended Data

---

[1]Department of Physiology, University of Pennsylvania Perelman School of Medicine, Philadelphia, PA, USA. [2]The Pennsylvania Muscle Institute, University of Pennsylvania Perelman School of Medicine, Philadelphia, PA, USA. [3]Howard Hughes Medical Institute, Janelia Research Campus, Ashburn, VA, USA. [4]Cell and Molecular Biology Graduate Group, University of Pennsylvania Perelman School of Medicine, Philadelphia, PA, USA. [5]Department of Dermatology, University of Pennsylvania Perelman School of Medicine, Philadelphia, PA, USA. [6]Department of Biochemistry, Stanford University, Stanford, CA, USA. [7]Institute of Neuronal Cell Biology, Technische Universität München, Munich, Germany. [8]Department of Biology, University of Washington, Seattle, WA, USA. [9]Howard Hughes Medical Institute, University of Washington, Seattle, WA, USA. ✉e-mail: holzbaur@pennmedicine.upenn.edu

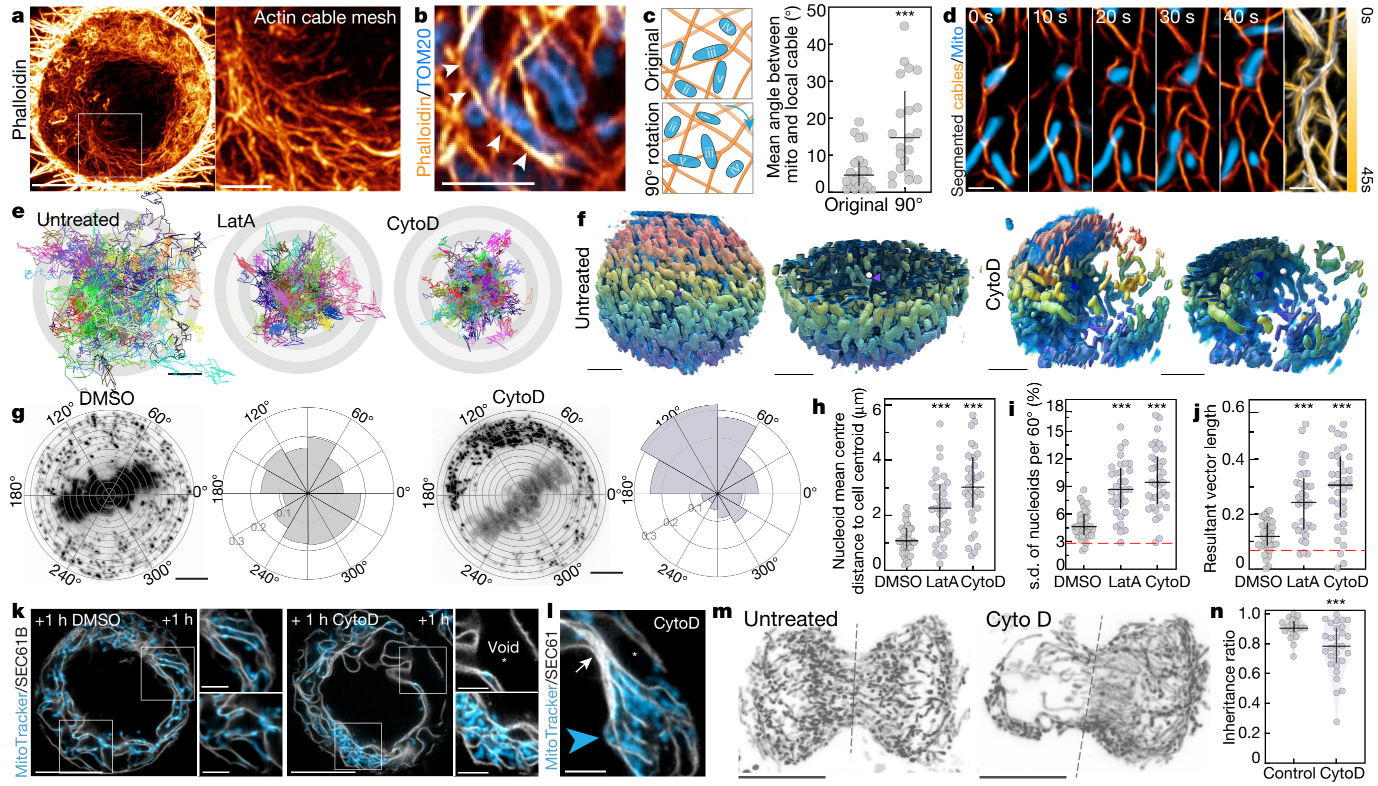

Fig. 1 | A subcortical actin meshwork scaffolds mitochondria and the ER in mitosis. a, Gamma-adjusted (0.5) maximum-intensity projection of a phalloidin-labelled metaphase HeLa cell. The bound region is expanded (right), highlighting the cytoplasmic actin cable meshwork. **b**, TOM20-labelled mitochondria align with neighbouring phalloidin-stained actin cables (arrowheads). **c**, Local co-orientation of mitochondria and neighbouring cables is lost upon 90° rotation of mitochondrial image. **d**, Time series of mitochondria and segmented cables with psuedocoloured time projection, indicating cable movement. **e**, Origin-aligned 60-s trajectories of 150 mitochondria from untreated, LatA-treated or CytoD-treated metaphase cells. **f**, Representative renderings with colour-coded *z* position of mitochondria in untreated or CytoD-treated metaphase HeLa cells; full-cell and half-cell views. **g**, PicoGreen staining of mtDNA nucleoids in DMSO- or CytoD-treated metaphase cells, with polar histograms indicating angular distribution. **h**, Distance from nucleoid mean centre position to cell centroid is increased upon actin cable disruption. **i**, **j**, Standard deviation of nucleoid percentage per 60° sector (**i**) and mean resultant vector length of nucleoid circular distribution (**j**) increase upon cable disruption. Red lines indicate values from simulations of uniformly positioned nucleoids. **k**, ER (Halo–SEC61B) and mitochondrial networks (MitoTracker) in metaphase HeLa treated with DMSO or CytoD. Asterisk indicates expanded inter-cisternal voids. **l**, Metaphase cable disruption induces stacked, collapsed ER sheets (eGFP–SEC61B, white arrow) and expanded inter-sheet voids (asterisk) that both exclude mitochondria (MitoTracker, blue arrowhead). **m**, Mitochondria (mito-dsRed2) in untreated or CytoD-treated (100 nM) telophase HeLa cells. Dashed line indicates cleavage plane. **n**, Mitochondrial inheritance ratio is decreased in CytoD-treated cells. Scale bars: 10 µm (**a**, **k**, **m**); 2.5 µm (**a** inset, **b**, **k** inset, **l**); 1 µm (**d**); 0.5 µm (**e**); 5 µm (**f**, **g**). Sample sizes: 19 cells (**c**); 36 DMSO, 33 LatA, 35 CytoD (**h**–**j**); 22 control, 29 CytoD (**n**). All samples were drawn from at least three independent experiments. Statistical tests: two-tailed Mann–Whitney test, $^{***}P = 0.0005$ (**c**); ordinary one-way analysis of variance (ANOVA) with Dunnett's multiple comparisons test, $^{***}P < 0.0001$ (**h**–**j**); two-tailed unpaired *t*-test, $^{***}P = 0.0008$ (**n**). Data are median ± interquartile range.

Fig. 3l–s). Similar defects in nucleoid positioning were observed in mitotic A549, HEK 293T and induced pluripotent stem cells (iPS cells) treated with CytoD (Extended Data Fig. 3t–v), suggesting that actin scaffolding of mitotic mitochondrial networks is conserved among symmetrically dividing mammalian cells.

We hypothesized that the altered mitochondrial positioning and motility induced by actin cable loss could be a result of increased confinement of mitochondria by the endoplasmic reticulum (ER), which closely associates with mitochondria via tethering proteins[10]. In metaphase, the ER adopts a loosely packed sheet-like morphology[11], with mitochondria positioned in close alignment with the curvilinear edges of the ER and actin cables threaded through the cytoplasmic voids between adjacent ER cisternae (Extended Data Fig. 4a–d). Disruption of actin cables resulted in ER collapse, with compaction of ER sheets and expansion of inter-cisternal cytoplasmic voids (Fig. 1k, Extended Data Fig. 4e–q, Supplementary Video 2). Mitochondria were excluded from both collapsed ER stacks and expanded voids, concentrating within pockets of the network (Fig. 1k, l, Extended Data Fig. 4r–v). Thus, we propose that the actin meshwork functions as a semi-rigid mechanical support that scaffolds mitochondria and associated ER membranes within the metaphase cytoplasm; loss of this scaffold induces progressive ER sheet-to-sheet compaction and resultant mitochondrial distribution defects.

We hypothesized that the irregular mitochondrial positioning that we observed in metaphase cells lacking actin cables would induce asymmetrical inheritance of mitochondrial mass between daughters. In control cells, we observed even apportionment of mitochondria at cytokinesis, whereas CytoD treatment induced asymmetric mitochondrial inheritance (Fig. 1m, n). Similar defects in mitochondrial inheritance were previously observed in cells depleted of myosin 19[7] (MYO19), suggesting that this mitochondrially localized actin motor may tether mitochondria to actin cables. MYO19 depletion did not eliminate actin cables but instead induced uncoupling of mitochondria from the meshwork, as well as ER collapse similar to that induced by cable disassembly (Extended Data Fig. 5a–m). Thus, maintenance of normal metaphase ER morphology may require close associations between ER cisternae and mitochondria transiently tethered to a semi-rigid actin meshwork by MYO19.

Actin cables were observed throughout the metaphase cytoplasm, but the most prominent subcortical actin features observed in live cells were revolving actin clusters (Extended Data Fig. 6a, b), as initially identified by Nishida and colleagues[12]. These mitotic actin clusters[12] appear remarkably similar to interphase mitochondrial actin waves that circle the nucleus[13] with a period of about 15 min (Extended Data Fig. 6c–g). To explore whether these cytoskeletal assemblies might be related, we tracked mitochondrial actin waves from interphase to mitosis. In all cells examined, the actin wave persisted through the G2/M transition, increasing in frequency and speed owing to enhanced rates of filament assembly and disassembly on metaphase mitochondria (Fig. 2a–f, Supplementary Video 3). In metaphase, about 80% of waves displayed processive unidirectional cycling, moving clockwise or anticlockwise with equal probability (Fig. 2g, Supplementary Video 4). Mitochondrial actin waves continued through all stages of mitosis before stalling on mitochondria at the cleavage furrow at cytokinesis; cycling subsequently reinitiated at slower interphase rates in each daughter cell (Extended Data Fig. 6h, Supplementary Video 3).

Close inspection of the actin wave revealed it is primarily composed of F-actin clouds surrounding individual mitochondria (Fig. 2h–j); similar actin clouds were not found on other organelles (Extended Data Fig. 6i–l). In phalloidin-labelled cells, clouds were threefold brighter than cables outside of the wave (Extended Data Fig. 7a–d, Supplementary Video 5). Clouds were characterized by a symmetrical nodal organization that develops over about 100 s; mitochondria within clouds displayed restricted motility (Fig. 2k, l, Extended Data Fig. 7e, f).

We tracked the fate of 290 actin clouds and identified multiple outcomes. Cloud disassembly was the most common outcome, and was marked by the progressive loss of nodes and resumption of normal diffusive mitochondrial motility (Fig. 2m, n). Unexpectedly, 13% of actin clouds underwent abrupt symmetry-breaking events, resulting in directed bursts of mitochondrial motion (Fig. 2n, o). In these events, we observed a gap form between adjacent nodes in the mitochondrial actin cloud that expanded over several seconds until the previously trapped organelle was actively propelled through the opening by the rapid and sudden elongation of actin comet tails (Fig. 2p, Extended Data Fig. 7g–j, Supplementary Video 6).

Mitochondrially associated actin comet tails exhibit a contrail-like morphology with twin tails emanating from attachment points close to the front of the organelle (Fig. 2q–r). Mitochondria were propelled at a speed proportional to the rate of comet tail extension, often travelling 5 µm or more (Fig. 2s, Supplementary Video 7). Comet tails were observed in multiple mitotic cell lines and were resolvable behind 96% of directed long-range mitochondrial movements (Fig. 2t, Extended Data Fig. 7l). In contrast to vesicular actin comet tails[14,15], mitochondrial comet tails promote highly linear and directed motion (Fig. 2u, Extended Data Fig. 7m–o, Supplementary Video 7), more closely resembling motility induced by comet tails assembled onto intracellular pathogens such as *Listeria*[16], *Rickettsia*[17] and *Shigella*[18]. The elongated, contrail-like tails associated with mitotic mitochondria most closely resemble comet tails nucleated by the *Rickettsia* protein Sca2[19].

Polarized comet tails often displayed a helical geometry, consistent with mitochondrial rotation during movement (Fig. 2v). About half of mitochondria (47%) were displaced in a direction opposite of the cycling wave (Fig. 2w, x), indicating that induction of comet tail motility but not its directionality is coupled to the actin wave. Comet tails occasionally regained symmetry, forming clouds that arrested mitochondrial movement (Extended Data Fig. 7p). More frequently, comet tails propelled mitochondria out of the plane of imaging (Extended Data Fig. 7q–t). Mitochondria associated with comet tails move at speeds consistent with actin-based motility[20] and persist in the absence of microtubules or MYO19 (Extended Data Fig. 7u–x). Thus, mitochondria associated with actin cables, clouds and comet tails displayed unique motility signatures (Fig. 2y, z, Extended Data Fig. 7y, z), suggesting that distinct actin assemblies in the deep metaphase cytoplasm differentially regulate mitochondrial positioning and movement.

To elucidate the assembly mechanisms of mitochondrially associated actin structures, we screened inhibitors of the actin cytoskeleton for effects on actin wave size (Extended Data Fig. 8a, b). Inhibitors of RHO and RAC GTPases predictably altered subcellular actin organization but did not inhibit actin assembly on mitochondria. Inhibition of ROCK or myosin II modestly reduced wave area. By contrast, inhibition of CDC42, its effector N-WASP or the ARP2/3 complex significantly decreased actin wave assembly. The pan-formin inhibitor SMIFH2 also impaired wave assembly, although the specificity of this inhibitor has been questioned[21]. To extend these observations, we performed a small interfering RNA (siRNA) screen of multiple actin binding proteins (Extended Data Fig. 8c–f). ARP3 depletion completely eliminated actin waves, but despite the effects induced by the N-WASP inhibitor wiskostatin, we did not observe a reduction in wave size upon depletion of N-WASP or other nucleation-promoting factors (NPFs) including WAVE1, WASH1 or WHAMM, which may reflect functional redundancy among NPFs or the existence of a yet-unidentified wiskostatin-sensitive NPF on mitochondria responsible for recruiting and activating ARP2/3.

Depletion of the actin elongator VASP significantly inhibited mitochondrial actin waves (Extended Data Fig. 8c). Live imaging and immunocytochemistry identified recruitment of VASP and other actin-binding proteins to mitochondrially associated F-actin (Extended Data Fig. 8g–n). Whereas depletion of the mitochondrially localized actin nucleator SPIRE1C[22] inhibited the wave, knockdown of its ER-localized interaction partner INF2[23] resulted in increased wave size, consistent with observations that this formin accelerates actin disassembly[24]. Depletion of three major actin-severing proteins—ADF (also known as DSTN), gelsolin and cofilin—induced a significant increase in wave area (Extended Data Fig. 8c), further suggesting that disassembly is required to maintain wave integrity.

Next, we analysed mitochondrial distribution, motility and inheritance in cells lacking actin waves. ARP3 depletion most effectively eliminated waves, inducing the complete loss of mitochondrial comet tails without disrupting subcortical actin cables (Extended Data Fig. 9a, b). Mitochondria in ARP3-depleted cells remained aligned with local actin cables, were uniformly distributed throughout the cytoplasm, and exhibited diffusive motility (Extended Data Fig. 9c–g, Supplementary Video 8). Although we observed moderately reduced total mitochondrial network exploration of cytoplasmic space, ARP3 depletion did not induce ER collapse or defects in mitochondrial mass inheritance (Extended Data Fig. 9h–m).

We observed that actin waves shuffle the relative positions of mitochondria within the mother cell (Extended Data Fig. 9n). As mitochondria vary in their genome, proteome, age and health[25–27], we hypothesized that spatial randomization would ensure that each daughter inherits a similar complement of mitochondria during symmetric cell divisions. To explore this, we focally damaged a region of the mitochondrial network at the start of mitosis and examined the dispersion of damaged mitochondria in the presence or absence of an actin wave. We double-labelled control or ARP3-depleted HeLa cells with the mitochondrially targeted photosensitizer mito-KillerRed and mitochondrially targeted photoactivatable GFP, then irradiated a region of about 100 µm^2 to simultaneously damage and photolabel a mitochondrial subpopulation (Fig. 3a, Supplementary Video 9). In control cells, we observed progressively increasing angular spread of the damaged mitochondria. By contrast, dispersion of damaged mitochondria was markedly reduced in ARP3-depleted cells or in cells treated with the ARP2/3 inhibitor CK-666 (Fig. 3a–e, Extended Data Fig. 10a–f). Reduced spread was not a by-product of mitochondrial damage and was not affected by depleting factors required for mitochondrial fusion (Extended Data Fig. 10g–n). These findings support the hypothesis that actin-based motility shuffles mitochondrial positioning during mitosis

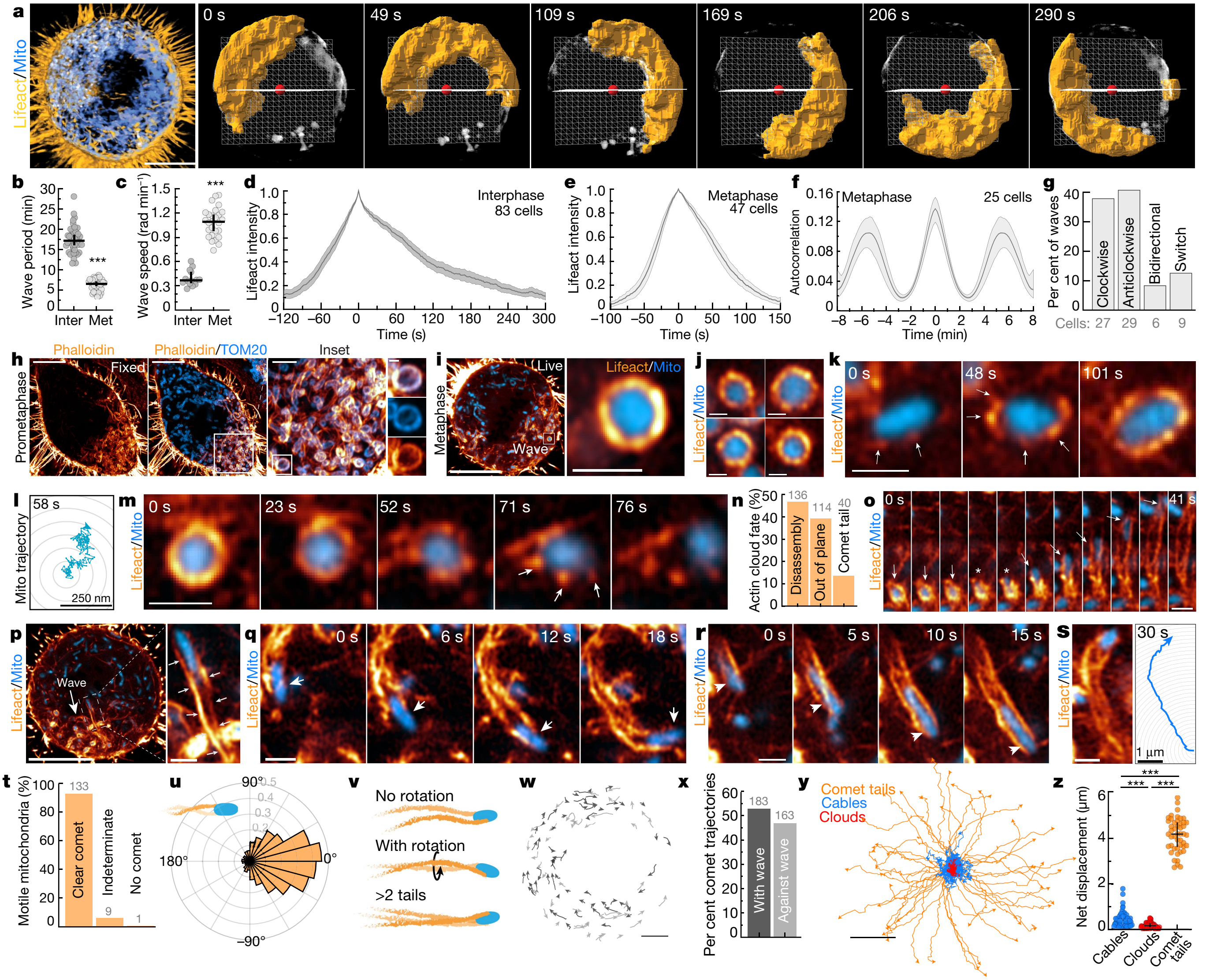

Fig. 2 | Mitochondrial actin clouds break symmetry to form elongated comet tails. a, Lattice light-sheet rendering of mito–dsRed2 and Lifeact–eGFP in a metaphase HeLa cell, with 3D segmentation of the mitochondrial actin wave over about 5 min. **b**, **c**, Actin wave period (**b**) and rotational speed (**c**) in interphase and metaphase. **d**, **e**, Kinetics of actin wave assembly and disassembly in interphase (**d**) or metaphase (**e**) cells. **f**, Autocorrelation analysis of metaphase actin waves. **g**, Directionality of metaphase actin waves. **h**, Airyscan image of a fixed prometaphase HeLa cell stained with phalloidin and labelled for TOM20, with magnified insets showing actin assembly on mitochondria. **i**, Live metaphase HeLa cells expressing Lifeact–eGFP and mito–dsRed2; magnified region shows a mitochondrial actin cloud. **j**, Representative mitochondrial actin clouds. **k**, Time series of actin cloud assembly on a mitochondrion. Arrows indicate actin nodes. **l**, Trajectory of a cloud-associated mitochondrion. **m**, Time series of actin cloud disassembly. Arrows indicate actin nodes. **n**, Percentage of clouds that disassemble, move out-of-plane or break symmetry to form a comet tail. **o**, Mitochondrial cloud-to-comet tail transition. Arrows, mitochondrial position; asterisks, symmetry-breaking event. **p**, Mitochondrial actin wave with inset showing mitochondrial actin comet tail (arrows). **q**, **r**, Representative actin comet tails driving directed mitochondrial movements (arrows). **s**, Mitochondrial comet tail with associated trajectory over 30 s. **t**, Percentage of motile mitochondria in metaphase cells with either clear, indeterminate or absent comet tails. **u**, Direction change between each step of mitochondrial comet-tail trajectories. **v**, Schematic illustrating mitochondrial comet-tail morphologies observed. **w**, Comet-tail-driven mitochondrial trajectories in metaphase HeLa. **x**, Percentage of comet-tail-based mitochondrial trajectories oriented with or against the direction of the actin wave. **y**, Origin-aligned trajectories of cable-, cloud- and comet-tail-associated mitochondria over 25 s. **z**, Net displacement of mitochondria associated with each actin structure over 25 s. Scale bars: 10 µm (**a**, **h**, **i**, **p**); 5 µm (**w**); 2.5 µm (**h**, inset); 2 µm (**y**); 1 µm (**i**, inset, **j**, **k**, **m**, **o**, **p**, inset, **q**–**s**); 500 nm (**h**, inset 2); 250 nm (**l**). Sample size: 41 interphase cells, 37 metaphase cells (**b**); 47 comet tails (**v**); 59 cables, 47 clouds, 59 comet tails (**z**). All samples were drawn from at least three independent experiments. Median ± interquartile range (**b**, **c**, **z**); mean ± 95% confidence interval (**d**–**f**). Statistical tests: two-tailed unpaired *t*-test, $^{***}P < 0.0001$ (**b**, **c**); Kruskal–Wallis test with Dunn's multiple comparisons test, $^{***}P < 0.0001$ (**z**).

to promote the dispersion of locally damaged organelles and increase the likelihood of even inheritance by daughter cells.

To further test the 'shuffling' hypothesis, we used experimentally derived parameters to simulate actin-based mitochondrial movement in mitosis (Fig. 3j, Supplementary Video 10) and the spreading of a focally 'damaged' subpopulation of mitochondria; we observed similar dispersion in simulated and experimental datasets (Fig. 3g). Increasing the duration of mitosis, actin wave size or comet tail velocity all increased mitochondrial mixing, suggesting that multiple parameters can be tuned to randomize mitochondrial position (Fig. 3h, i, Extended Data Fig. 10o–q).

Finally, we used the simulation to query the effect of the actin wave on mitochondrial inheritance. Daughter cells inherited equivalent mitochondrial mass in simulations with or without the actin wave,

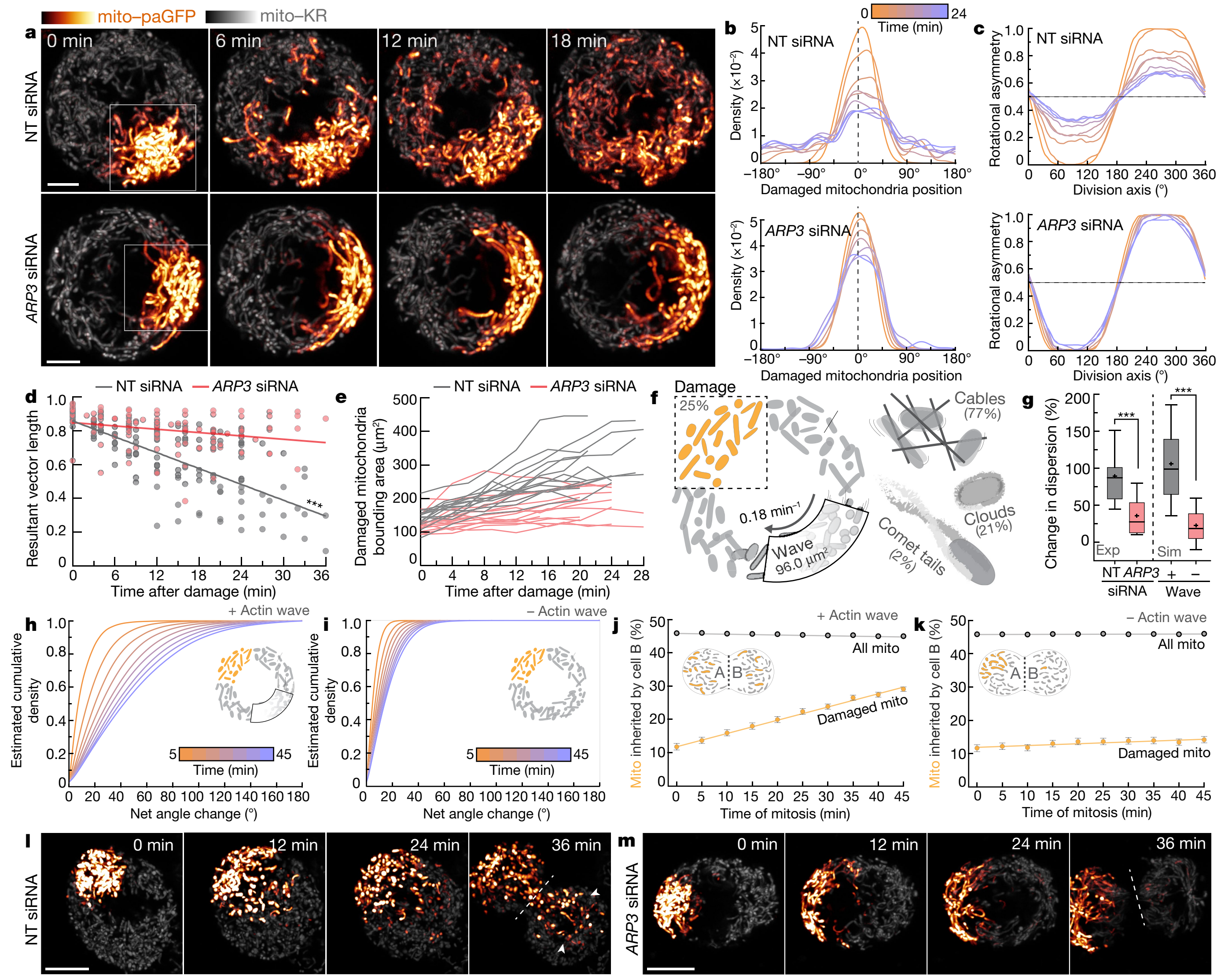

Fig. 3 | Actin waves disperse clusters of damaged mitochondria. a, Time series of metaphase HeLa cells expressing mito-KillerRed (mito–KR) and mito-photoactivatable GFP (mito–paGFP) and treated with either non-targeting (NT) siRNA (top) or *ARP3* siRNA (bottom). Boxes identify regions irradiated with 405 nm and 561 nm light to simultaneously bleach mito–KR and activate mito–paGFP to focally damage and label the same organelle subpopulation. **b**, Representative estimates of distribution of circular density of damaged mitochondria over time in NT siRNA-treated (top) or *ARP3* siRNA-treated (bottom) metaphase cells. Dashed line indicates mean angular position of damaged mitochondria at 0 min. **c**, Rotational asymmetry plots of damaged mitochondria in NT (top) or *ARP3* (bottom) siRNA-treated metaphase cells (Methods). **d**, Resultant vector length of damaged mitochondria over time in NT or *ARP3* siRNA-treated HeLa cells with linear regression lines. **e**, Bounding area of damaged mitochondria in NT or *ARP3* siRNA-treated metaphase cells. **f**, Schematic indicating parameters used for simulation. **g**, Left, experimentally derived change in dispersion of damaged mitochondria in NT or *ARP3* siRNA-treated cells between 0 and 15 min. Right, simulated change in dispersion of damaged mitochondria over 15 min in the presence or absence of actin waves. **h**, **i**, Cumulative density estimations of net angular displacement of damaged mitochondria over time in simulations with (**h**) or without (**i**) actin waves. **j**, **k**, Percentage of damaged and total mitochondria inherited by daughter cell B in simulations with (**j**) or without (**k**) actin waves. **l**, **m**, Time series showing mito–KR and mito–paGFP in cells treated with NT siRNA (**l**) or *ARP3* siRNA (**m**). Dashed line indicates cleavage plane, arrows indicate damaged mitochondria inherited by cell B. Scale bars: 10 μm (**a**, **l**, **m**). Sample sizes: 13 NT, 15 *ARP3* (**d**); 15 NT, 15 *ARP3* (**e**, **g**). All samples were drawn from at least three independent experiments. Statistical tests: slopes significantly unequal, extra sum-of-squares *F* test, ***$P < 0.0001$ (**d**); two-tailed Mann–Whitney test, ***$P < 0.0001$. Centre line shows median, box encompasses the interquartile range, whiskers span 10th to 90th percentiles and '+' indicates the mean (**g**); mean ± 95% confidence interval (**j**, **k**).

consistent with the experimental data (Fig. 3j, k, Extended Data Fig. 9l, m). However, cells with simulated waves were more likely to evenly distribute damaged mitochondria between daughters, an effect that increased over longer durations of mitosis, faster comet speeds or larger actin waves (Fig. 3j, k, Extended Data Fig. 10r, s). Consistent with modelling, experimental data revealed that focally damaged mitochondria were more likely to be evenly split between daughters in control cells compared with ARP3-depleted cells lacking comet tail-based mitochondrial motility (Fig. 3l, m).

In summary, we applied super-resolution imaging to define fundamental mechanisms in which actin dynamics control mitochondrial organization and inheritance in symmetrically dividing animal cells. We identified three distinct cytoplasmic actin assemblies with complementary roles in organizing mitochondria during mitosis. First, actin cables form a 3D meshwork that scaffolds mitochondria and the ER to maintain their uniform distribution. Next, we used advanced microscopy to identify previously observed actin clusters[12] as a wave of F-actin assembly and disassembly on mitochondria. Within this wave, most mitochondria are encased within actin clouds, which can spontaneously break symmetry to form polarized comet tails. Mitochondrial comet tails, analogous to those propelling intracellular bacterial pathogens[16–19], drive directed bursts of actin-based motility that shuffle mitochondrial positioning. This shuffling randomizes mitochondrial position, increasing the likelihood that each daughter receives functionally equivalent mitochondrial networks.

In asymmetrically dividing cells, functionally distinct mitochondria are unequally apportioned to influence daughter cell fate[26,28]. By contrast, symmetric cell division is intended to produce identical daughter cells of comparable fate, an outcome necessary for the continual regeneration of epithelia to maintain tissue homeostasis[29]. In this context, preventing unequal inheritance may avoid fate divergence, clonal expansion of deleterious mtDNA mutations, or metabolic heterogeneity[29,30]. The actin-based mixing mechanism described here represents a solution to this problem: just as a card dealer shuffles a deck of cards to guarantee each player receives a fair hand, the actin wave can shuffle mitochondria within the mother cell to guarantee that each daughter cell is dealt a random and equitable inventory of mitochondria.

Online content

Any methods, additional references, Nature Research reporting summaries, source data, extended data, supplementary information, acknowledgements, peer review information; details of author contributions and competing interests; and statements of data and code availability are available at https://doi.org/10.1038/s41586-021-03309-5.

1. Carlton, J. G., Jones, H. & Eggert, U. S. Membrane and organelle dynamics during cell division. *Nat. Rev. Mol. Cell Biol.* **21**, 151–166 (2020).
2. Taguchi, N., Ishihara, N., Jofuku, A., Oka, T. & Mihara, K. Mitotic phosphorylation of dynamin-related GTPase Drp1 participates in mitochondrial fission. *J. Biol. Chem.* **282**, 11521–11529 (2007).
3. Kashatus, D. F. et al. RALA and RALBP1 regulate mitochondrial fission at mitosis. *Nat. Cell Biol.* **13**, 1108–1115 (2011).
4. Chung, J. Y., Steen, J. A. & Schwarz, T. L. Phosphorylation-induced motor shedding is required at mitosis for proper distribution and passive inheritance of mitochondria. *Cell Rep.* **16**, 2142–2155 (2016).
5. Altmann, K., Frank, M., Neumann, D., Jakobs, S. & Westermann, B. The class V myosin motor protein, Myo2, plays a major role in mitochondrial motility in *Saccharomyces cerevisiae*. *J. Cell Biol.* **181**, 119–130 (2008).
6. Simon, V. R., Swayne, T. C. & Pon, L. A. Actin-dependent mitochondrial motility in mitotic yeast and cell-free systems: identification of a motor activity on the mitochondrial surface. *J. Cell Biol.* **130**, 345–354 (1995).
7. Rohn, J. L. et al. Myo19 ensures symmetric partitioning of mitochondria and coupling of mitochondrial segregation to cell division. *Curr. Biol.* **24**, 2598–2605 (2014).
8. Field, C. M. & Lénárt, P. Bulk cytoplasmic actin and its functions in meiosis and mitosis. *Curr. Biol.* **21**, R825–R830 (2011).
9. Kita, A. M. et al. Spindle-F-actin interactions in mitotic spindles in an intact vertebrate epithelium. *Mol. Biol. Cell* **30**, 1645–1654 (2019).
10. Salvador-Gallego, R., Hoyer, M. J. & Voeltz, G. K. SnapShot: functions of endoplasmic reticulum membrane contact sites. *Cell* **171**, 1224–1224 (2017).
11. Lu, L., Ladinsky, M. S. & Kirchhausen, T. Cisternal organization of the endoplasmic reticulum during mitosis. *Mol. Biol. Cell* **20**, 3471–3480 (2009).
12. Mitsushima, M. et al. Revolving movement of a dynamic cluster of actin filaments during mitosis. *J. Cell Biol.* **191**, 453–462 (2010).
13. Moore, A. S., Wong, Y. C., Simpson, C. L. & Holzbaur, E. L. Dynamic actin cycling through mitochondrial subpopulations locally regulates the fission–fusion balance within mitochondrial networks. *Nat. Commun.* **7**, 12886 (2016).
14. Taunton, J. et al. Actin-dependent propulsion of endosomes and lysosomes by recruitment of N-WASP. *J. Cell Biol.* **148**, 519–530 (2000).
15. Kast, D. J., Zajac, A. L., Holzbaur, E. L., Ostap, E. M. & Dominguez, R. WHAMM directs the Arp2/3 complex to the ER for autophagosome biogenesis through an actin comet tail mechanism. *Curr. Biol.* **25**, 1791–1797 (2015).
16. Tilney, L. G. & Portnoy, D. A. Actin filaments and the growth, movement, and spread of the intracellular bacterial parasite, *Listeria monocytogenes*. *J. Cell Biol.* **109**, 1597–1608 (1989).
17. Heinzen, R. A., Hayes, S. F., Peacock, M. G. & Hackstadt, T. Directional actin polymerization associated with spotted fever group *Rickettsia* infection of Vero cells. *Infect. Immun.* **61**, 1926–1935 (1993).
18. Bernardini, M. L., Mounier, J., d'Hauteville, H., Coquis-Rondon, M. & Sansonetti, P. J. Identification of icsA, a plasmid locus of *Shigella flexneri* that governs bacterial intra- and intercellular spread through interaction with F-actin. *Proc. Natl Acad. Sci. USA* **86**, 3867–3871 (1989).
19. Haglund, C. M., Choe, J. E., Skau, C. T., Kovar, D. R. & Welch, M. D. *Rickettsia* Sca2 is a bacterial formin-like mediator of actin-based motility. *Nat. Cell Biol.* **12**, 1057–1063 (2010).
20. Theriot, J. A., Mitchison, T. J., Tilney, L. G. & Portnoy, D. A. The rate of actin-based motility of intracellular *Listeria monocytogenes* equals the rate of actin polymerization. *Nature* **357**, 257–260 (1992).
21. Nishimura, Y. *et al*. The formin inhibitor, SMIFH2, inhibits members of the myosin superfamily. Preprint at https://doi.org/10.1101/2020.08.30.274613 (2020).
22. Manor, U., Bartholomew, S., Golani, G. & Christenson, E. A mitochondria-anchored isoform of the actin-nucleating spire protein regulates mitochondrial division. *eLife* **4**, e08828 (2015).
23. Korobova, F., Ramabhadran, V. & Higgs, H. N. An actin-dependent step in mitochondrial fission mediated by the ER-associated formin INF2. *Science* **339**, 464–467 (2013).
24. Chhabra, E. S. & Higgs, H. N. INF2 Is a WASP homology 2 motif-containing formin that severs actin filaments and accelerates both polymerization and depolymerization. *J. Biol. Chem.* **281**, 26754–26767 (2006).
25. Vincent, A. E. et al. Subcellular origin of mitochondrial DNA deletions in human skeletal muscle. *Ann. Neurol.* **84**, 289–301 (2018).
26. Katajisto, P. et al. Stem cells. Asymmetric apportioning of aged mitochondria between daughter cells is required for stemness. *Science* **348**, 340–343 (2015).
27. Aryaman, J., Hoitzing, H., Burgstaller, J. P., Johnston, I. G. & Jones, N. S. Mitochondrial heterogeneity, metabolic scaling and cell death. *BioEssays* **39**, 1700001 (2017).
28. McFaline-Figueroa, J. R. et al. Mitochondrial quality control during inheritance is associated with lifespan and mother-daughter age asymmetry in budding yeast. *Aging Cell* **10**, 885–895 (2011).
29. Rué, P. & Martinez Arias, A. Cell dynamics and gene expression control in tissue homeostasis and development. *Mol. Syst. Biol.* **11**, 792 (2015).
30. Stewart, J. B. & Chinnery, P. F. Extreme heterogeneity of human mitochondrial DNA from organelles to populations. *Nat. Rev. Genet.* **22**, 106–118 (2020).

Methods

No statistical methods were used to predetermine sample size. The experiments were not randomized. The investigators were not blinded to allocation during experiments and outcome assessment.

Materials

Plasmids. Plasmids used were: pLenti-PGK.Lifeact-eGFP:W (Addgene, 51010), F-tractin-eGFP (Addgene, 58473), F-Tractin (ITPKA)-mNeonGreen (Addgene, 98883), mScarlet-I-UtrCH (Addgene, 98823), Lifeact-mScarlet-N1 (Addgene, 85054), Lifeact-mNeonGreen (Addgene, 98877), Rab7a-eGFP, SKL-eGFP, Halo-KDEL and Halo-Sec61b (gifts from C. Obara, Janelia Research Campus), Emerald-Sec61b (Addgene, 90992), pKillerRed-dMito (Evrogen, PF964), mito-paGFP (Addgene, 23348), mito-Dendra2 (Addgene, 55796), mito-dsRed2 (gift from T. Schwarz, Harvard Medical School), mito-mTagBFP2 (Addgene, 105011), pLV-mitoGFP (Addgene, 44385), Emerald-FilaminA-N-9 (Addgene, 54098), Emerald-Cortactin-C-12 (Addgene, 54051), Emerald-VASP-5 (Addgene, 54296) and AlphaActinin-mNeonGreen (Allele biotech).

Dyes. Dyes used were: MitoTracker Red CMXRos (100 nM; CST, 9082), MitoTracker Deep Red FM (100 nM; Invitrogen, M22426), TMRE (30 nM; Life Technologies, T-669), SiR-Lysosome (1 μM; Cytoskeleton, CY-SC012), SiR-Actin (1 μM; Cytoskeleton, CY-SC001), PicoGreen dsDNA Reagent (1:10,000; Invitrogen, P7581), Hoechst 33342 (1:1,000; Invitrogen, H3570), Hoechst 34580 (1:1,000; Invitrogen, H21486), Alexa Fluor 488 Phalloidin (1:40; Invitrogen, A12379), Alexa Fluor 555 Phalloidin (1:40; Invitrogen, A34055), Alexa Fluor 568 Phalloidin (1:40; Invitrogen, A12380), CellMask Orange (1:2,000; Invitrogen, C10045), JF635-HaloLigand (100 nM; gift from L. Lavis, Janelia Research Campus).

Antibodies. Primary antibodies used were: anti-alpha-tubulin clone DM1A (Sigma, T6199), anti-TOM20 (Abcam, ab78547), anti-TOM20 F-10 (SantaCruz, sc-17764), anti-HSP60 LK1 (SantaCruz, sc-59567), anti-filamin 1 E-3 (SantaCruz, sc17749), Anti-ARP3 (Proteintech, 13822-1-AP), anti-cofilin E-8 (SantaCruz, sc-376476), anti-gelsolin GS-2C4 (Abcam, ab11081), anti-ADF (Abcam, ab186754), anti-cortactin 4F11 (Millipore, 05-180), anti-pericentrin (Biolegend, 923701), anti-INF2-CAAX and pan-INF2 (gifts from H. Higgs, Geisel School of Medicine, Dartmouth), anti-N-WASP (CST, 4848T), anti-VASP (CST, 3112), anti-WASHC1 (Atlas, HPA002689), anti-WAVE1 (SantaCruz, sc-271507), anti-WHAMM (Abcam, ab122572), anti-myosin19 (Abcam, ab174286) and anti-MyoVa (SantaCruz, sc-365986). Secondary antibodies used were: goat-anti-rabbit Alexa Fluor 555 (Invitrogen, A-21429), donkey-anti-rabbit AlexaFluor 594 (Invitrogen, R37119), donkey-anti-rabbit Alexa Fluor 647 (Invitrogen, R37119), goat anti-mouse Alexa Fluor 488 (Invitrogen, A-11001), goat-anti-mouse Alexa Fluor 594 (Invitrogen, A11032), goat-anti-mouse, Alexa Fluor 647 (Invitrogen, A32728), IRDye 800CW donkey anti-rabbit (Licor, 926-32213) and IRDye 800CW Donkey anti-mouse (Licor, 926-32212).

siRNA. siRNAs used were: ON-TARGETplus Non-targeting siRNA #1 (Dharmacon, D-001810-01-20), Myosin 19 (SantaCruz, sc93640), MyoVa (SantaCruz, sc-35995), INF2-CAAX (Dharmacon, ACAAAGAAACUGUGUGUGAUU), INF2 (Santa Cruz, sc-92159), N-WASP (Dharmacon: #1 AAGAAAAGAAGAAGGGAAAUU, #2 CAACUUAAAGACAGAGAAAUU), VASP (SantaCruz, sc- 29516), WASHC1 (Dharmacon, J-190043-(01-04)-0002), WAVE1 (SantaCruz, sc-29516), WHAMM (Dharmacon, L-022415-01), ARP3 (Santa Cruz, sc-29739), Cofilin 1 (CST, 6267S), ADF (SantaCruz, sc- 43200), Gelsolin (SantaCruz, sc-37330), Spire1C (Dharmacon, CCUAGGAUAACCAGUGUAUUU), MFN1 (Santa Cruz, sc-43927) and MFN2 (Santa Cruz, sc-43928).

Cell culture

Cells used were: HeLa-M (A. Peden, University of Sheffield), HaCaT (ATCC), COS-7 (ATCC), ARPE19 (ATCC), HEK 293T (ATCC), PTK2 (ATCC), U2OS (ATCC), RPE1 (Janelia Cell Biology Core), MDA-MB-231 (D. Matus, Stony Brook University), and A549 (O. Quintero, University of Richmond) cells were cultured in DMEM with 4.5 g l^{-1} glucose (Corning, 10-017-CM), 2 mM GlutaMAX (Gibco, 35050061) and 10% FBS. HeLa-M and HEK 293T were authenticated by STR profiling and tested negative for mycoplasma. Twenty-four to forty-eight hours before imaging, cells were seeded on 35-mm glass-bottom dishes with no. 1.5 cover glass (MatTek, P35G-1.5-C-C). The human WTC11 iPS cell line was a gift from M. Ward at the National Institutes of Health[31]. iPS cells were maintained on hESC-qualified Matrigel (Corning) and fed daily with Essential 8 medium (Thermo Fisher). The day before transfection, iPS cells were dissociated into single cells with Accutase (STEMCELL Technologies) and plated on imaging dishes (Mattek) at 0.3×10^6 cells per dish in Essential 8 medium containing the ROCK inhibitor Y-27632 (10 μM, Tocris). The next day, medium was exchanged to Essential 8 without ROCK inhibitor.

Embryonic day 18 (E18) rat hippocampal neurons were obtained from the Neuron Culture Service Center at the University of Pennsylvania and plated at a density of 333 neurons per mm^2 on poly-L-lysine-coated (GIBCO) 35-mm glass-bottom dishes (P35G-1.5-20-C; MatTek) and grown in Neurobasal (GIBCO) supplemented with 2% B-27 (GIBCO), 58 mM glucose (Sigma), 2 mM GlutaMAX (GIBCO), 100 U ml^{-1} penicillin and 100 mg ml^{-1} streptomycin (Sigma). Cells were maintained at 37 °C in a 5% CO$_2$ water-jacketed incubator.

Normal human epidermal keratinocytes (NHEKs) were isolated from discarded, de-identified neonatal human foreskin by a 12-h incubation at 4 °C in 2.4 U ml^{-1} dispase II[32]. The underlying dermis was removed, followed by incubation in 0.25% Trypsin at 37 °C for 10 m before neutralization in 1 ml FBS. Cells were dissociated by mechanical scraping, and the resulting cell suspension was passed through a 40-μm strainer. Cells were then centrifuged at 200*g* for 5 min and resuspended in 5 ml M154 (Invitrogen) containing 0.07 mM calcium.

Organotypic raft cultures

Epidermal differentiation can be modelled using organotypic 'raft' cultures. In short, J2 3T3 fibroblasts were embedded within a matrix of type 1 collagen to form a solid raft in the upper chamber of a Transwell dish. A confluent monolayer of NHEKs was then seeded on top of the raft. NHEKs monolayers were grown at an air–liquid interface by adding liquid medium to the bottom chamber of the Transwell dish. In this system, the NHEKs stratify within seven days to form the normal histological layers of the epidermis, including fully cornified cells[2]. Coupling organotypic cultures with stable retroviral expression of mito–dsRed2 allowed us to examine the dynamics of mitochondria in metaphase NHEKs within a live, three-dimensional and physiological context (Extended Data Fig. 1e).

Drug treatments

Drugs used were: CK-666 (200 μM, 1 h; Sigma, SML0006), latrunculin A (1 μM, 0–2 h; Sigma, L5163), cytochalasin D (100 nM, 1–2 h; Sigma, C2618), DMSO (1–3 h; Sigma, D2650), nocodazole (10 or 25 μM, 1 h; Sigma, M1404). EHT1864 (20 μM, 1 h; Tocris), rhosin hydrochloride (100 μM, 1 h; Tocris), C3 transferase (2 μg ml^{-1}, 3 h; Cytoskeleton), Y27632 (10 μM, 1 h; Sigma), blebbistatin (85 μM, 1 h; Sigma), ML141 (25 μM, 1 h; Millipore Sigma), wiskostatin (10 μM, 1 h; TOCRIS), SMIFH2 (25 mM, 1 h; Sigma), U0126 (20 μM, 1 h; 19-147, EMD Millipore), and Erlotinib (1 μg ml^{-1}, 1 h; SML2156, Sigma).

Transient transfection

For transient transfection of HeLa-M, COS-7, HEK 293T, A549 and HaCaTs, plasmid DNA was complexed with FuGENE 6 (Promega, E269A) at a 1:3 ratio in 100 μl Opti-MEM (Gibco, 31985-070). After a 10-min incubation, the transfection solution was added to cells, which were imaged 18–36 h later. siRNA transfection was performed using 40 nM siRNA complexed with Lipofectamine RNAiMAX in Opti-MEM

(ThermoFisher). Cells were imaged about 48 h post-transfection. For transfection of iPS cells, 2 µg plasmid DNA was incubated with 10 µl Lipofectamine Stem (Thermo Fisher) and 200 µl OptiMEM for 10 min and added dropwise to the dish. Cells were imaged 24 h after transfection. Neurons were transfected at 2 days in vitro (DIV2) with 1 µg total DNA (0.5 µg mito–dsRed2, 0.5 µg Lifeact-eGFP) and 1 µl Lipofectamine 2000 (Invitrogen) for 30 min and imaged 16 h later.

Stable cell generation

Lentivirus was generated by transient transfection of HEK 293T cells seeded in 10-cm cell culture plates with psPAX2 (Addgene), VSV-G (Addgene) and transfer plasmid. At 48–72 h post-transfection, the supernatant was collected, cellular debris was removed by low-speed centrifugation, and the viral supernatant was added to cells. Cells were incubated with virus for 4–24 h before two complete media changes. Alternatively, Phoenix 293 cells (courtesy of G. Nolan, Stanford Univ.) were used to produce replication-deficient amphotropic retrovirus. The pLZRS retroviral packaging vector encoding fluorophore-tagged proteins within the multi-cloning site was used to transfect sub-confluent Phoenix cells grown in DMEM with 10% heat-inactivated FBS (DMEM/hiFBS) in a 60-mm plate. Transfection was carried out using 4 µg of pLZRS DNA combined with 12 µl of FuGene-6 transfection reagent in 800 µl Opti-MEM, which was added to the cells for 18 h at 37 °C. Phoenix cells were then passaged in DMEM/hiFBS containing 1 µg ml^{-1} puromycin to select for those harbouring the pLZRS construct. After 48 h, puromycin was removed and replaced with fresh DMEM/hiFBS for 24 h at 32 °C. The supernatant containing retrovirus was collected, centrifuged at 200*g* for 5 min to remove any Phoenix cells, then aliquots were snap-frozen in liquid nitrogen for long-term storage. Thawed retroviral supernatants with 4 µg ml^{-1} polybrene added were used to replace the medium on sub-confluent mammalian cells in 10-cm culture plates at 37 °C for 1–24 h depending on the cell type. After the transduction, the viral supernatant was removed, and mammalian cells were washed with PBS, then cultured and passaged in their normal medium. One week after viral transduction, fluorescence activated cell sorting was used to isolate single, low- to medium-expressing clones. Monoclonal HeLa-M colonies expressing Lifeact–Scarlet, Lifeact–eGFP and Lifeact–eGFP with mito–dsRed2 were generated.

Western blots

Cells were pelleted and then lysed in RIPA buffer (50mM Tris-HCl pH 7.4, 150mM NaCl, 1% Triton X-100, 0.5% deoxycholate, 0.1% SDS) supplemented with protease inhibitors for 30 min on ice. After lysis, samples were centrifuged at 17,000*g* at 4 °C for 10 min and the supernatant was collected. Total protein in the lysates was determined by BCA assay (ThermoFisher Scientific). Samples were subjected to SDS–PAGE and then transferred onto FL PVDF membrane.

Membranes were probed with the following primary antibodies: INF2-CAAX and pan-INF2 (gifts from H. Higgs, Geisel School of Medicine, Dartmouth, 1:1,000), N-WASP (Cell Signaling Technology, 4848T, 1:1,000), VASP (Cell Signaling Technology, 3112, 1:1,000), WASHC1 (Atlas, HPA002689, 1:1,000), WAVE1 (Santa Cruz Biotechnology, sc-271507, 1:200), WHAMM (abcam, ab122572, 1:250), ARP3 (Proteintech, 13822-1-AP, 1:1,000), ADF (Abcam, ab186754, 1:1,000), cofilin (Santa Cruz Biotechnology, sc-376476, 1:1,000), gelsolin (Abcam, ab11081, 1:1,000), Myo19 (Abcam, ab174286, 1:2,000), MyoVa (Santa Cruz, sc-365986, 1:500). Then, blots were visualized with fluorescent secondary antibodies (Li-Cor) on an Odyssey CLx imaging system.

Blots were analysed with Image Studio. In place of blotting for a loading control, we used a quantitative fluorescent total protein stain (LI-COR Biosciences). For each lane, the background was subtracted and pixel intensity values were summed. Comparison of these sums enabled determination of relative amounts of protein loaded in each gel well. Normalization factors were applied to measurements on immunoblots in calculating per cent knockdown and are shown in representative images as 'relative total protein'. Per cent knockdown calculations reflect the results of at least three independent experiments.

Live imaging

For the majority of live-imaging experiments, cells were imaged in their culture media (complete DMEM) at 37 °C and 5% CO_2. A subset of short-term (<30 min) spinning-disk videos were acquired at 37 °C and ambient CO_2. Overnight spinning disk time-lapse experiments as well as all experiments on the lattice light-sheet microscope were performed in L-15 (Gibco, 11415-064) supplemented with 10% FBS, 100 U ml^{-1} penicillin and 100 mg ml^{-1} streptomycin (Sigma). Hippocampal neurons were imaged in Hibernate E (Brain bits). Live imaging experiments were performed on two spinning disk confocal microscopes (SDCMs) (SDCM no. 1: Perkin Elmer UltraVIEW VOX, SDCM no. 2 Yokogawa CSU-X1), a Zeiss LSM 880 with Airyscan (Zeiss), a VT iSIM (Biovision), a custom grazing-incidence structured illumination microscope (GI-SIM; Lippincott-Schwartz lab), a Leica SP8 Falcon with a stimulated emission depletion (STED) microscope or a custom lattice light-sheet microscope (Janelia).

Immunocytochemistry

Cells cultured on 35-mm glass-bottom dishes were fixed in fresh 4% PFA (Electron Microscopy Services, 15710-S) or 4% PFA + 0.2% glutaraldehyde (Electron Microscopy Services, 160000) for 10 min and subsequently washed 3 times in PBS. Fixed cells were then permeabilized in 0.2% Triton X-100 for 5 min (if staining membrane proteins) or 0.5% Triton X-100 in PBS for 10 min (if staining cytoskeleton alone), before blocking in 3% BSA in PBS for 10 min at room temperature. For Fig. 1a, cells were pre-extracted with 0.25% (v/v) Triton X-100 and 0.3% glutaraldehyde (v/v) in cytoskeleton buffer for 90 s before a 10 min fixation in 2% glutaraldehyde in cytoskeleton buffer[33]. Glutaraldehyde-induced autofluorescence was quenched by 5 min incubation in freshly prepared 0.1% (w/v) sodium borohydride (Sigma, 452882), followed by a 30 min incubation in PBS with 3% w/v BSA and 0.5% w/ Triton X-100. For tracking experiments on fixed mitochondria (Extended Data Fig. 7z), cells were fixed in 2% glutaraldehyde in cytoskeleton buffer for 10 min, washed 2 times in PBS and imaged immediately. Cells were incubated with primary antibodies (1:50–1:500) for 1–3 h at room temperature or overnight at 4 °C in PBS with 3% BSA. After primary antibody incubation, cells were washed several times in PBS and incubated with Alexa Fluor secondary antibodies (1:200–1:1,000) for 1 h. Immediately before imaging, cells were incubated with 1:40 Alexa Fluor-labelled Phalloidin for 45 min. Fixed cells were imaged in PBS.

Expansion microscopy

Expansion microscopy (Extended Data Fig. 1f) was performed using an adapted protocol from Chozinski et al., 2016[34]. After immunocytochemistry was performed as described above, fixed and stained cells in 35-mm MatTek dishes were incubated with 200 µl of 0.25% (v/v) glutaraldehyde in PBS for 10 min. Cells were then washed 3 times in 1× PBS and incubated in 200 µl monomer solution (1× PBS, 2 M NaCl, 2.5% (w/w) acrylamide, 0.15% (w/w/) *N*,*N*′-methylenebisacrylamide, 8.6% (w/w) sodium acrylate) for 1 min. Monomer solution was removed and replaced with 50 µl of gelation solution (1.06× monomer solution, 0.2% (w/w) TEMED, 0.2% (w/w) APS) and wells were enclosed with coverslips for 30 min. Gels were then incubated with digestion buffer for 30 min before expansion in 50 ml deionised water. 4× expanded gels were images on the iSIM using 60×/1.2 NA water objective.

Camera-based systems

Spinning disk confocal microscopy. SDCM was performed on one of two systems. SDCM no. 1 was a Nikon Eclipse Ti inverted scope equipped with PerkinElmer UltraVIEW VOX confocal system (Perkin Elmer) and an EM-CCD camera (Hamamatsu) housed within a 37 °C environment chamber. Cells were excited with 405-nm, 488-nm, 561-nm and 640-nm laser lines, and emission was collected using either a 100×/1.49 NA apochromat total internal reflection fluorescence (TIRF) objective (Nikon) or 60×/1.4 NA plan apochromat oil immersion objective (Nikon) with standard emission filter sets. Images were acquired with Volocity acquisition software (Perkin Elmer). *z*-stacks were acquired using a piezo motor and step sizes of either 100 nm or 150 nm, requiring ~200–300 steps to fully sample rounded, metaphase cells. 3D image stacks were deconvolved with Huygens Professional v.19.04 (Scientific Volume Imaging) with the CMLE algorithm and signal-to-noise ratio between 20 and 30, maximum of 40 iterations, and stopping criterion of 0.01. SDCM no. 2 was a Nikon TiE inverted microscope equipped with a spinning-disk scan head (Yokogawa, CSU-X1) and an EM-CCD camera (iXon Ultra 897). Imaging was performed with standard laser lines with fluorescence emission collected by a 100×/1.49 NA apochromat TIRF objective (Nikon). Images were acquired with NIS-Elements AR v.4.40.00 (Nikon). Cells were incubated within a Tokai Hit stage top incubator at 37 °C and 5% CO_2.

Instant structured illumination microscopy. Instant structured illumination microscopy (iSIM) images were acquired on a Visitech VT iSIM mounted on an Olympus IX71 inverted microscope with a LCI Chamlide stagetop incubation system (37 °C, 5% CO_2) housed within the University of Pennsylvania's Cell and Developmental Biology imaging core. Samples were excited with 488-nm, 561-nm and 640-nm laser lines and images were collected with a Hamamatsu ORCA Flash 4.0 sCMOS camera. Images were acquired with either an Olympus UPlanSAPO 60×/1.2 NA water immersion objective or a UPlanSAPO 100×/1.4 NA oil immersion. Images were acquired with Metamorph v.7.10.1.161. iSIM images were manually de-striped in imageJ using a notch filter.

Grazing incidence structured illumination microscopy. GI-SIM was performed on a custom-built microscope[35] with a 100×/1.49 NA objective (Olympus) in a 37 °C, 5% CO_2 live imaging chamber. Samples were illuminated with 488/561-nm lasers lines and emission was detected by an ORCA-Flash 4.0 sCMOS camera (Hamamatsu) with *xy* pixel size 0.03955 µm. Images were acquired with LabView software. SIM processing was performed using custom software. Channel alignment was performed on images of TetraSpeck Microspheres (ThermoFisher; T14792) using the descriptor-based registration (2D/3D) plugin[36] in Fiji and a rigid 2D transformation model.

Lattice light-sheet microscopy. The lattice light-sheet microscope used here is housed in the Advanced Imaging Center at the Howard Hughes Medical Institute Janelia research campus. The system is configured and operated as previously described[37]. HeLa cells were seeded on 5 mm round glass coverslips and grown for 24–48 h (Warner Instruments, catalogue no. CS-5R). Samples were illuminated by a 2D optical lattice generated by a spatial light modulator (Fourth Dimension Displays). The sample was excited by 488- nm or 560- nm diode lasers (MPB Communications) through an excitation objective (Special Optics, 0.65 NA, 3.74-mm WD). Fluorescent emission was collected by detection objective (Nikon, CFI Apo LWD 25×W, 1.1 NA), and detected by a sCMOS camera (Hamamatsu Orca Flash 4.0 v2). Acquired data were deskewed as described[37] and deconvolved using an iterative Richardson–Lucy algorithm. Point-spread functions for deconvolution were experimentally measured using 200-nm tetraspeck beads adhered to 5-mm glass coverslips (Invitrogen, T7280) for each excitation wavelength.

Laser-scanning confocal microscopes

Airyscan microscopy. Airyscan microscopy was performed on an inverted Zeiss LSM 880 equipped with an Airyscan module. Samples were excited with standard laser lines (405- nm, 488- nm, 561- nm and 633- nm) and imaged with either a plan apochromat 63×/1.4 NA DIC M27 oil objective or a 40×/1.2 NA C-apochromat water objective (Zeiss). Two-colour (488- nm and 561- nm) high-speed videos (2-4 fps) were acquired using line-scanning mode with 1-, 2-, 4- or 8-line averaging and a 495–550- nm bandpass/570- nm longpass emission filter. *z*-stacks were acquired using a piezo-motor and Nyquist-optimized *z* step sizes. Live imaging was performed at 37 °C and 5% CO_2. Images were acquired and processed using automatic 2D or 3D Airyscan processing in ZEN software (Zeiss).

STED microscopy. STED microscopy was performed on an inverted TCS SP8 STED 3x (Leica) with a pulsed white-light laser with tunable excitation from 470 to 670- nm. Live Halo–KDEL-expressing HeLa cells (Extended Data Fig. 4f) were labelled with JF635-HaloLigand (100 nM) and maintained at 37 °C and 5% CO_2. Sample was excited with 633-nm light and depletion was carried out with a pulsed nanosecond 775-nm depletion laser. Images were collected with an HC PL APO 86×/1.2 NA water objective (Leica). Images were acquired and processed using LAS X software (v.3.1.5.16308).

Image analysis

Depth colour-coded maximum-intensity projections. Depth colour-coded maximum-intensity projections were generated in Fiji[38] using the Colorize stack.ijm macro (https://github.com/ndefrancesco/macro-frenzy) to pseudocolour *xy* stacks by slice number using the perceptually uniform Turbo look up table (https://ai.googleblog.com/2019/08/turbo-improved-rainbow-colormap-for.html) generated for ImageJ (https://github.com/cleterrier/ChrisLUTs). Stacks were then resliced starting at the bottom, and the Grouped *z* Project function was used to create 3.7-µm maximum-intensity projections.

Actin cable renderings. Actin cable renderings in Extended Data Fig. 1b, c were generated from automatically processed 3D Airyscan stacks (Zen Black, Zeiss). Cortical actin signal was removed in Fiji by tracing a line approximately 500 nm beneath the cortex in each 2D slice and using the 'clear outside' function. Processed stacks were then imported into Imaris 9.5.0 (BitPlane) and rendered using either a shadow projection, with light sources positioned to backlight the cables (Extended Data Fig. 1b), or a blend projection (Extended Data Fig. 1c).

Actin cable segmentation. Actin cable segmentation in Extended Data Fig. 1e was generated by manually tracing a 3D phalloidin-stained metaphase HeLa in Amira (ThermoFisher), exporting the results to ImageJ (NIH), and applying a depth-coded maximum-intensity projection. Cables (Fig. 1d, Extended Data Fig. 1s) were segmented using a ridge detector[39] from the Ridge detection plugin (https://doi.org/10.5281/zenodo.594213) in Fiji with sigma values between 1 and 8, depending on signal-to-noise, minimum line length of 6 pixels to avoid erroneous branching, 'extend line' selected, and method for overlap resolution set to 'none'. Binary cables were then time-averaged with a 5-frame mean filter (2 s total), thresholded to remove erroneous detections, and filtered with a 1-pixel gaussian blur to simulate cable widths from the real images. Cables were psuedocoloured with the glow LUT in Fiji.

Actin cable orientation mask. Actin cables in Extended Data Fig. 1f were segmented using a ridge detector as described above, followed by the skeletonize function to generate skeletons of the cable long axis. Orientation maps of the segmented cables were generated in the Fiji plugin OrientationJ[40], using a cubic spline gradient with gaussian window sigma = 2 pixels. NaN-background 32-bit cable skeletons were then multiplied by the orientation maps using the image calculator function to calculate the local orientation at each pixel of the cable mesh. The spectrum LUT was used to pseudocolour cables by orientation, before converting to RGB and applying a 1-pixel gaussian blur to simulate cable width.

Cable width analysis. Actin cable widths (Extended Data Fig. 1i) were analysed in processed GI-SIM videos of Lifeact–eGFP in the basal cytoplasm of metaphase HeLa cells. One-pixel line scans were drawn orthogonally to the long axis of the cables and full width at half maximum was determined by gaussian fitting. Parallel measurements were carried out on processed GI-SIM images of 100-nm tetraspeck beads (ThermoFisher).

Actin mesh pore size analysis. Actin mesh pore size (Extended Data Fig. 1j, k) was estimated by first segmenting actin cables using a ridge detector as described above. Binary images were then inverted, effectively segmenting the inter-cable pores, and the distance map function was used to calculate the distance from each pixel in the actin pore to the nearest cable. In MATLAB, the maximum eroded point of the cable pore segmentation was multiplied by the distance map to calculate the average pore radius. Note: only pores completely within the region of interest (ROI) were analysed: pores centres at the edges of the ROI were automatically filtered out. Maximum pore circle fit was defined as the square of the largest pore radius per cell multiplied by π.

Actin cable 2D density. Cable density (Extended Data Fig. 1l) was calculated on 5 × 5 µm ROIs drawn entirely within the cytoplasm of phalloidin-stained metaphase or anaphase HeLa cells. The segmented line tool was then used to manually trace all actin cables visible in the window. The total length of the actin cables (µm) was then divided by the area of the ROI (25 μm^2) to determine the cable length per unit area (µm per μm^2).

Mitochondria–cable orientation analysis. Mitochondria–cable orientation analysis (Fig. 1c) was performed on approximately 4 × 4 µm square ROIs generated from 2D images of Lifeact–eGFP and mito–dsRed2 in the basal cytoplasm of metaphase HeLa cells. Mitochondria and cable long axes were manually segmented using the segmented line tool. Orientation maps of segmented cables and mitochondria were generated in OrientationJ using a cubic spline gradient (gaussian window = 2 pixels). In MATLAB, 32-bit NaN-background mitochondria masks were multiplied by mitochondria orientation maps to calculate the local orientation of all mitochondrial pixels in the ROI. In parallel, mitochondria masks were also multiplied by actin cable orientation maps to calculate the orientation of actin cables nearest each mitochondrial pixel. As orientations are axial data, running from only −90° to 90°, all orientations were multiplied by a 2× correction factor before calculating the mean angle difference between each mitochondrial pixel and its nearest cable neighbour using the circ_dist function in the MATLAB CircStat package[41]. Average angular differences were then divided by two to back calculate relative orientation differences. As a control, the mitochondria mask was rotated 90° and a new orientation map was generated. Thirty-two-bit NaN-background 90° rotated mitochondria masks were then multiplied by their own orientation map as well as the original actin cable orientation map, to calculate the relative orientation of shifted mitochondria and their new neighbouring cables.

Two-dimensional metaphase mtDNA nucleoid distribution analyses. Nucleoid distribution analyses (Fig. 1h–j, Extended Data Fig. 3l–s) were performed on 2D images of metaphase HeLa cells acquired approximately 10–12 µm above the coverslip. In ImageJ, chromosomal PicoGreen staining was manually segmented and subtracted from the image. Next, the Find Maxima process was used to identify point coordinates for each nucleoid. Finally, the polygon selection tool was used to trace the perimeter of the cell, and the *xy* position of the cell centroid was determined using the Measure command. The *xy* nucleoid coordinates were exported to MATLAB. Nucleoid mean centre-to-cell-centroid distance (Fig. 1h) was determined by averaging the *x* and *y* positions of all nucleoids in the cell. This value was then subtracted from the *xy* position of the cell centroid, and the absolute value was reported as the mean centre-to-cell-centroid distance. To carry out radial and angular nucleoid analyses, *xy* coordinates were converted to polar coordinates about the centroid using the cart2pol function. The s.d. of per cent nucleoids per 60° circle sector (Fig. 1i) was determined using a custom MATLAB script in which the percentage of nucleoids was calculated for each of 6 × 60° circle sectors. Resultant vector length (Fig. 1j) was determined using the CircStats package in MATLAB[41]. Nucleoid rotational asymmetry analyses (Extended Data Fig. 3m–o) were performed using a custom MATLAB script in which the cell is bisected by a dividing chord splitting the cell into equal size semicircles: side A and side B. The dividing chord is then revolved 360° and the proportion of nucleoids on side A (that is, side A/(side A + side B)) was computed at 1° intervals from 0° to 360°. The resulting curve (shown in Extended Data Fig. 3n) is antisymmetric around 180° with a mean rotational asymmetry value of 0.5. Lower rotational asymmetry variance values indicate more uniform nucleoid positioning. Average Euclidean and circular nearest-neighbour distances between each nucleoid and its ten nearest neighbours was calculated in MATLAB using pdist2, and the variance-to-mean ratio (index of dispersion) was plotted. For all nucleoid circular distribution analyses (Fig. 1i, j, Extended Data Fig. 3o, r), we performed Monte Carlo simulations of nucleoids drawn from uniform circular distributions to approximate the expected output given true circular uniformity (mean values are shown as red dashed lines).

Cytokinesis inheritance ratio. Analyses were performed on summed intensity projections of mito–dsRed2-expressing cytokinetic HeLa cells. The daughter cell with a smaller mitochondrial network was defined as cell A. Inheritance ratio was calculated as mitochondrial mass in Cell A divided by mass in Cell B. A value of 1 indicates equal inheritance.

3D Mitochondrial mass distribution analysis. Deconvolved spinning disk (Extended Data Fig. 3g–k) or lattice light-sheet (Fig. 1f) stacks of metaphase mito–dsRed2-expressing cells were rendered and segmented in Imaris 9.4.0. The Surfaces tool was used with the Shortest Distance Calculation option selected. Surface detail was set at 0.01 µm with Smooth selected. Background subtraction (local contrast) was used with the diameter of largest sphere which fits into the object set to 0.5 µm. The threshold was manually adjusted to mask all mitochondrial signal, and the 'Split touching objects (region growing)' option was selected with seed points diameter = 0.75 µm. Seed points were filtered on the basis of quality to remove spurious detections or mitochondria outside of the metaphase cell. The segmentation mask was then statistics coded based on *z* position (Jet colormap) and an organic texture map was applied. The mask was then superimposed on a volume rendering (blend) of the raw data for display (Fig. 1f, Extended Data Fig. 3g). The Cartesian coordinates of mitochondrial centre points were exported from Imaris into MATLAB. There, the 3D mitochondrial mean centre point was determined by averaging the *x*, *y* and *z* coordinates. And the mitochondrial mean centre distance to the cell centroid was reported (Extended Data Fig. 3i). Cell centroids are indicated in Fig. 1f as spheres and mitochondria mean centre positions are indicated by prisms. Cartesian centre point coordinates were then converted to spherical coordinates about the cell centroid using the MATLAB cart2sph function. Spherical coordinates were converted from radians to degrees with azimuth range 0° to 360° and elevation range −90° to 90°. Note: 90° elevation corresponds to the top of the cell, 0° corresponds to the equator, and −90° corersponds to the bottom of the cell (Extended Data Fig. 3g). The s.d. of mitochondrial mass per wedge (Extended Data Fig. 3j) was calculated by dividing the cell into 6 equal sized spherical wedges (3 below the equator, 3 above the equator, each 120° wide), and the percentage of points in each wedge was determined. The s.d. of per cent occupancy for each wedge was plotted. 3D resultant vector length (Extended Data Fig. 3k) was performed in MATLAB using elevation and azimuth as previously described[42]

Inter-cisternal ER void analyses. Curvilinear ER-sheet profiles in mitotic HeLa cells were segmented using the ridge detector workflow previously used to segment actin cables. Inter-cisternal ER void size and centre positions were determined using the identical workflow to identify actin meshwork pore centres (Extended Data Fig. 4j–q). Mean distance from void centre to nearest mitochondria (Extended Data Fig. 4u) was performed by binarizing mitochondria images in Fiji, generating distance maps representing the distance of all background pixels to the nearest mitochondrion, and, in MATLAB, multiplying the Euclidean distance maps of the mitochondria by binary images of the void centres.

Two-dimensional mitochondrial mass distribution analysis. Binary segmentations of metaphase mitochondria (mito–dsRed2) after DMSO, CytoD, NT siRNA, *MYO19* siRNA (Extended Data Fig. 5) or *ARP3* siRNA treatment (Extended Data Fig. 9) were generated using the pixel classification workflow in ilastik[43]. Binaries were then imported to MATLAB and the mean *xy* position of the mitochondrial network was calculated and the distance between this value and the centroid of the cell (identified in Fiji on the basis of the cortical actin signal) was plotted (Extended Data Figs. 5d, 9f). Once in MATLAB, the binary mask was also converted from Cartesian coordinates to polar coordinates about the cell centroid using cart2pol. The percentage of mitochondrial mass in each 60° sector was calculated as was done with the nucleoids. The standard deviation of the per cent mass occupancy was then plotted (Extended Data Figs. 5e, 9f).

Three-dimensional segmentation of actin wave. Segmentation of the actin wave from lattice light-sheet videos (Fig. 2a) was accomplished using a custom Hydra Image Processor[44] within MATLAB. Cortical actin and retraction fibres were removed using a cytoplasmic mask derived from the mitochondria channel. The remaining diffusive actin signal was segmented. Each frame was reoriented using a principal component analysis.

Actin wave dynamics. Three-dimensional time projection of a metaphase actin wave (Extended Data Fig. 6b) was generated in Fiji by using the oval selection tool to draw a circle just inside of the metaphase cortex and using the 'clear outside' function to crop out the bright cortical actin signal. A 3D projection of the cropped actin was then generated using the '3D project' function. To determine the actin wave period (Fig. 2b), three ROIs were drawn in different regions of the cytoplasm in Fiji. Plot *z*-axis profile was then used to determine Lifeact intensity within these ROIs. Peaks were manually identified in the Lifeact trace for each box and the mean interpeak distance was calculated and averaged for all three ROIs to calculate mean periodicity. Angular wave speed (Fig. 2c) was determined by manually tracking the centroid of the actin wave using the angle tool in Fiji. Analyses of actin wave rise and fall time (Fig. 2d, e) were performed on cells imaged at 2 s per frame. In Fiji, 4-pixel line scans were drawn in cytoplasmic regions perpendicular to the plasma membrane. Plot *z*-axis profile was used to generate traces of actin intensity over time. Actin intensity traces were smoothed using Sovitsky-Golay filtering in MATLAB and intensity values were linearly rescaled from 0 to 1. Peaks were then manually aligned in Excel (Microsoft) such that max intensity values corresponded to $t = 0$. Aligned curves were then plotted in Prism 8 (GraphPad). The temporal autocorrelation of actin intensity (Fig. 2f, Extended Data Fig. 6d) was computed according to the standard definition of the unbiased estimate of the discrete autocorrelation function, implemented in MATLAB. To mitigate time-dependent fluctuations in background intensity, the varying baseline actin signal over time was corrected using msbackadj. Next, the unbiased temporal autocorrelation function was computed using the xcorr function. The mean and 95% confidence intervals for the autocorrelation signal were computed using bootstrapped resampling with 1,000 repeats. Actin wave directional bias (Extended Data Fig. 6e) was determined by tracking the position of the actin wave over 100 min (50 steps), and assigning clockwise steps values of +1, anticlockwise steps values of −1, and stationary events values of 0.

Actin wave area. Two-dimensional cross-sectional wave area (Extended Data Fig. 8a, c) was manually determined using the freehand selection tool and measure area function in Fiji.

Cable and cloud phalloidin intensity. Relative phalloidin intensity for actin clouds and cables (Extended Data Fig. 7d) was calculated by averaging the mean intensity of ten line scans drawn at the cell cortex, in the actin wave (clouds), or along actin cables. Intensity values for clouds and cables were divided by intensity of the cortical phalloidin. Of note, this analysis cannot be used to directly deduce total F-actin in each structure, as phalloidin accessibility may differ between these networks.

Mitochondria tracking. Mitochondria trajectories were generated using a semi-automated tracking workflow in the TrackMate[45] Fiji plugin. A Laplacian of Gaussian detector was used to identify mitochondria with an estimated blob diameter of 0.4–0.6 µm, a threshold value that minimized spurious detections (typically between 30 and 70) and sub-pixel localization. Remaining gaps or spurious localizations were manually corrected using the add or delete spot tool. The simple linear assignment problem tracker was then used to generate trajectories with linking max distance set to 0.5 µm, gap-closing max distance set to 0.5 µm, and gap-closing max frame gap set to 1. Tracks were filtered to remove incomplete trajectories or those that were clipped at the *x* or *y* edges of the image. Tracking was performed on Airyscan videos acquired at 500 ms per frame over 121 steps (Fig. 1) or 50 steps (Fig. 3). Origin-aligned tracks were randomly coloured and plotted using a custom MATLAB script. Mean squared displacement (MSD) and autocorrelations were computed in MATLAB using the msdanalyzer package[46]. Ensemble analysis of the mean squared displacements of mitochondria was performed using Bayesian MSD model fitting using the technique of Monnier et al.[47]. Automated tracking of glutaraldehyde-fixed mitochondria was used to estimate localization or tracking error. Discretized velocity autocorrelations (Extended Data Fig. 3f) were generated as previously described[48] using a custom MATLAB script courtesy of S. Weber (McGill University, Montreal).

Cumulative time projections and displacement index. Cumulative maximum intensity time projections of mitochondria in metaphase cells (Extended Data Fig. 9h) were generated using the *z*-project function in Fiji. Mitochondria signal was segmented using the pixel classification tool in ilastik and total mitochondrial area was calculated using the 'analyze particles' function in Fiji. Percentage of cell explored by mitochondria (Extended Data Fig. 9i) was calculated by dividing the mitochondrial area in 5-min cumulative projections by the total cell area. Displacement index (Extended Data Fig. 9j) was calculated as described previously[49] by dividing mitochondrial area in the 5-min cumulative projection by mitochondrial area in frame 1 at 0 min.

Damaged, photoactivated mitochondria dispersion analyses. Maximum-intensity projections of mito–paGFP were thresholded in Fiji using Otsu's method and binary masks were imported into MATLAB. A custom script was then used to convert *xy* positions of mitochondria pixels to polar coordinates and the circular mean of the mitochondrial position was calculated using the Circ Stats package[41]. Thresholded pixels were reoriented so that the angle of the circular mean was equal to 0° and all pixels were between −180° and 180° of that point. The angular distribution of mitochondrial mass at different time points (Fig. 3b, Extended Data Fig. 10h, n) was then plotted in MATLAB using a kernel smoothing density estimate for circular data (Vlad Atanasiu (2020), MATLAB Central File Exchange https://www.mathworks.com/matlabcentral/fileexchange/32614-kernel-smoothing-density-estimate-for-circular-data). Rotational asymmetry analysis (Fig. 3c) was performed by bisecting the cell with a dividing chord running through the mean angle of damaged mitochondria at time 0 (0°) and rotating the axis at 1° intervals over the entire circle (0°–360°) at each time point. Asymmetry was calculated as the mass of damaged mitochondria on side A divided by the total mass of damaged mitochondria in the cell (side A + side B). The progressively decreasing amplitude of the rotational asymmetry plot in NT siRNA-treated cells indicates increased dispersion and spatial uniformity of the damaged mitochondria. The mean rotational asymmetry over a half-turn of the bisecting chord (that is, 0°–180°) is reported in Extended Data Fig. 10d. The resultant vector length (Fig. 3d) of damaged mitochondria around the spindle was calculated using the circular statistics package in MATLAB[41]. The bounding area of damaged mitochondria (Fig. 3e) was calculated by manually circumscribing the activated paGFP in Fiji using the freehand selection tool. xy mass shift (Extended Data Fig. 10e) was determined by calculating the average xy position of binarized paGFP between each frame and dividing by the time interval.

Modelling actin dynamics

All data were generated from simulations written in MATLAB. This type of stochastic simulation, in which space is continuous and time is discrete, has been previously described[50]. In these simulations, mitochondria were simulated as a set of x–y coordinate pairs moving according to a random walk inside a mitotic circular cell containing a circular spindle in the centre. Mitochondria cannot move outside the cell or inside the spindle. Several parameters were set at the beginning of a simulation: the radius of the circular spindle (to create an area of approximately 131.4 μm^2), the radius of the cell (to create an area of approximately 551.6 μm^2), the percentage of the cell cytoplasm that the actin wedge occupies (approximately 96 μm^2), the speed of the actin wedge (approximately 1.15 rad s^{-1}), the number of mitochondria (92 total), the effective diffusion coefficient of mitochondria outside of the actin wedge (0.0046 $\mu m^2 s^{-1}$), and the effective diffusion coefficient of mitochondria associated with an actin comet tail (0.057 $\mu m^2 s^{-1}$). All these parameters were determined experimentally. The values of the diffusion coefficients were calculated to allow mitochondria to move with speeds of approximately 68 nm s^{-1} and 237 nm s^{-1}. Also, we simulate mitochondria photoconversion by labelling all mitochondria within a randomly selected 25% area of the cell. Photoconverted mitochondria were depicted as larger dots than non-photoconverted mitochondria.

Every run of the for loop is equivalent to 2 s, during which mitochondria move according to numbers sampled from the standard normal distribution scaled by the square root of $2D \times \Delta t$ where D is the effective one-dimensional diffusion coefficient, and Δt is 2 s. Mitochondria were forced to stay inside the cell but outside the spindle by resampling an angle from 0 to 2π if a particular step would make them enter these forbidden regions. All mitochondria outside of the wedge move with a speed of 68 nm s^{-1}. If a mitochondrion is inside a wedge, it has a 10% chance of growing a comet tail, at which point it will move with a speed of 237 nm s^{-1} and be perfectly persistent. The other 90% of mitochondria inside the wedge become immobile. Mitochondria retain an actin comet tail for 14 s only, that is, 7 steps of the for loop. After this time, the mitochondrion will become immobile if it is still inside the wedge, and another mitochondrion inside the wedge will grow an actin comet tail. We ran simulations for a total of 15 min (450 steps) and 30 min (900 steps). At the end of a simulation, $\Delta\theta$, that is, the radial displacement of a particular mitochondrion, was calculated for each photoconverted mitochondrion.

The cartoon schematic in Extended Data Fig. 4v was generated using BioRender.

Statistics and reproducibility

Statistical analysis and graphing were carried out using Prism 8.0 or MATLAB. Normality testing (D'Agostino–Pearson) was performed to determine whether to use parametric or non-parametric statistical tests. For the comparison of two datasets, normally distributed data were analysed by two-tailed unpaired Student's t-test, whereas non-normally distributed data were analysed by two-tailed Mann–Whitney test. To compare more than two normally distributed datasets, we used ordinary one-way ANOVA with either Dunnett's multiple comparisons (to compare the mean of each column with a control column) or Tukey's multiple comparisons test (to compare the mean of each column with every other column). To compare more than two non-normally distributed datasets, we used the Kruskal–Wallis test with two-sided Dunn's multiple comparison test.

All statistical analyses were performed on samples drawn from at least three independent experiments. All representative micrographs were selected from datasets from at least three independent experiments.

Reporting summary

Further information on research design is available in the Nature Research Reporting Summary linked to this paper.

Data availability

Source data are provided with this paper.

Code availability

MATLAB code used for analysing 3D mitochondrial distribution, 2D nucleoid distribution, ER void size and distribution, mitochondrial motility and damaged-mitochondria circular spread is available at https://github.com/andmoo91/CircularAnalyses_MatLab.

31. Fernandopulle, M. S. et al. Transcription factor-mediated differentiation of human iPSCs into neurons. *Curr. Protoc. Cell Biol.* **79**, e51 (2018).
32. Simpson, C. L., Kojima, S. & Getsios, S. RNA interference in keratinocytes and an organotypic model of human epidermis. *Methods Mol. Biol.* **585**, 127–146 (2010).
33. Xu, K., Zhong, G. & Zhuang, X. Actin, spectrin, and associated proteins form a periodic cytoskeletal structure in axons. *Science* **339**, 452–456 (2013).
34. Chozinski, T. J. et al. Expansion microscopy with conventional antibodies and fluorescent proteins. *Nat. Methods* **13**, 485–488 (2016).
35. Guo, Y. et al. visualizing intracellular organelle and cytoskeletal interactions at nanoscale resolution on millisecond timescales. *Cell* **175**, 1430–1442 (2018).
36. Preibisch, S., Saalfeld, S., Schindelin, J. & Tomancak, P. Software for bead-based registration of selective plane illumination microscopy data. *Nat. Methods* **7**, 418–419 (2010).
37. Chen, B.-C. et al. Lattice light-sheet microscopy: imaging molecules to embryos at high spatiotemporal resolution. *Science* **346**, 1257998 (2014).
38. Schindelin, J. et al. Fiji: an open-source platform for biological-image analysis. *Nat. Methods* **9**, 676–682 (2012).
39. Steger, C. An unbiased detector of curvilinear structures. *IEEE Trans. Pattern Anal. Mach. Intell*. **20**, 113–125 (1998).
40. Püspöki, Z., Storath, M., Sage, D. & Unser, M. Transforms and operators for directional bioimage analysis: a survey. *Adv. Anat. Embryol. Cell Biol*. **219**, 69–93 (2016).
41. Berens, P. CircStat: a MATLAB toolbox for circular statistics. *J. Stat. Softw*. **31**, https://doi.org/10.18637/jss.v031.i10 (2009).
42. Upton, G. & Mardia, K. Statistics of directional data. *J. R. Stat. Soc. A* **136**, 262–263 (1973).
43. Berg, S. et al. ilastik: interactive machine learning for (bio)image analysis. *Nat. Methods* **16**, 1226–1232 (2019).
44. Wait, E., Winter, M. & Cohen, A. R. Hydra image processor: 5-D GPU image analysis library with MATLAB and Python wrappers. *Bioinformatics* **35**, 5393–5395 (2019).
45. Tinevez, J.-Y. et al. TrackMate: an open and extensible platform for single-particle tracking. *Methods* **115**, 80–90 (2017).
46. Tarantino, N. et al. TNF and IL-1 exhibit distinct ubiquitin requirements for inducing NEMO-IKK supramolecular structures. *J. Cell Biol*. **204**, 231–245 (2014).
47. Monnier, N. et al. Bayesian approach to MSD-based analysis of particle motion in live cells. *Biophys. J*. **103**, 616–626 (2012).
48. Weber, S. C., Thompson, M. A., Moerner, W. E., Spakowitz, A. J. & Theriot, J. A. Analytical tools to distinguish the effects of localization error, confinement, and medium elasticity on the velocity autocorrelation function. *Biophys. J*. **102**, 2443–2450 (2012).
49. Quintero, O. A. et al. Human Myo19 is a novel myosin that associates with mitochondria. *Curr. Biol*. **19**, 2008–2013 (2009).
50. Ortega, F. E., Koslover, E. F. & Theriot, J. A. *Listeria monocytogenes* cell-to-cell spread in epithelia is heterogeneous and dominated by rare pioneer bacteria. *eLife* **8**, e40032 (2019).

Acknowledgements We thank M. Tokito, A. Stout and the UPenn Cell and Developmental Biology microscopy core, and F. Tuluc and the CHOP Flow Cytometry core for technical contributions; S. Weber for MATLAB code; O. Quintero and D. Matus for cell lines; H. Choi and B. Rossetti for advice on analyses; and M. Ostap, F. Cross, M. Moore, C. Evans, S. Cason, Y. Wong and O. Harding for critical feedback. This work was funded by support from NIH

R35 GM126950 and RM1 GM136511 to E.L.F.H., NIH F31 GM123644 and CHOP MitoRAG Pilot Grant to A.S.M., NIH R37 AI036929 and HHMI investigator support to J.A.T., and a HHMI Gilliam Fellowship to F.E.O. C.L.S. was supported by grants from NIAMS/NIH (K08 AR075846), the Dermatology Foundation, and the National Psoriasis Foundation. NHEKs were supplied by Penn SBDRC Core B supported by NIAMS/NIH (P30 AR069589). J.J.N. was supported by F30NS092227 and the UPenn NGG Hearst Fellowship. C.A.B. was supported by the German Research Foundation (DFG; BO 5434/1-1). J.L.-S. was supported by HHMI. The Advanced Imaging Center at the Janelia Research Campus is a jointly funded venture of the Gordon and Betty Moore Foundation and the Howard Hughes Medical Institute.

Author contributions A.S.M. and E.L.F.H. conceptualized the project and designed experiments. A.S.M performed imaging experiments, C.L.S. prepared and transduced isolated NHEK and organotypic NHEK cultures, S.M.C. performed western blots, J.M.H. assisted with lattice light-sheet experiments, P.G.-D. cultured and transfected primary hippocampal neurons, C.A.B. cultured and transfected iPS cells. A.S.M., J.J.N., E.C.W., S.M.C. and C.J.O. analysed data. E.C.W. designed custom image analysis suite to segment and visualize lattice light-sheet microscopy data. F.E.O. and J.A.T. designed and implemented simulations. A.S.M. designed the figures. T.-L.C., J.A.T. and J.L.-S. provided critical feedback. A.S.M. and E.L.F.H. wrote the paper and all authors contributed to revisions.

Competing interests The authors declare no competing interests.

Additional information
Supplementary information The online version contains supplementary material available at https://doi.org/10.1038/s41586-021-03309-5.
Correspondence and requests for materials should be addressed to E.L.F.H.
Peer review information *Nature* thanks Benedikt Westermann and the other, anonymous, reviewer(s) for their contribution to the peer review of this work. Peer reviewer reports are available.
Reprints and permissions information is available at http://www.nature.com/reprints.

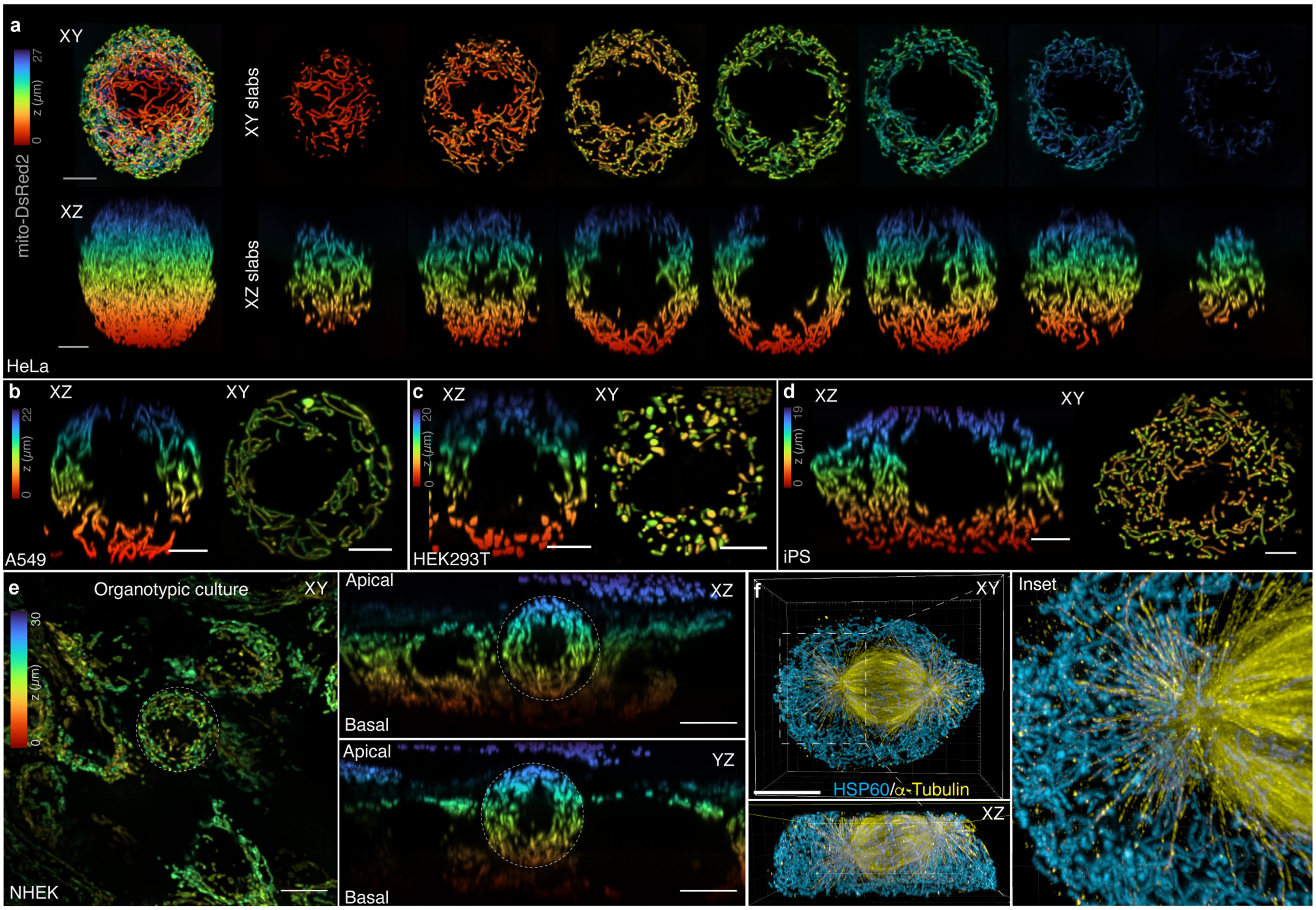

Extended Data Fig. 1 | Mitochondrial networks are uniformly distributed throughout the cytoplasm surrounding the mitotic spindle. a, *z*-coded *xy* and *xz* maximum-intensity projections of approximately 4-µm slabs through a live, metaphase HeLa cells expressing mito–dsRed2. Mitochondria are excluded from the spindle region and are uniformly distributed above, below, and around the spindle. **b**–**d**, *z*-coded *xy* and *xz* maximum-intensity projections of approximately 4 µm sections through the centre of A549 (**b**), HEK 293T (**c**) and iPS (**d**) cells expressing mito–dsRed2. **e**, *z*-coded *xy* (left) and *xz* (right) maximum-intensity projections of approximately 4-µm sections through the centre of a live, organotypic culture of NHEKs expressing mito–dsRed2. **f**, 4× expanded iSIM rendering of mitochondria (anti-HSP60) and microtubules (anti-α-tubulin) in a prometaphase HeLa cell. Mitochondria are entirely excluded from the spindle and show limited overlap with astral microtubules. Scale bars: 5 µm (**a**–**d**), 10 µm (**e**), 40 µm (**f**).

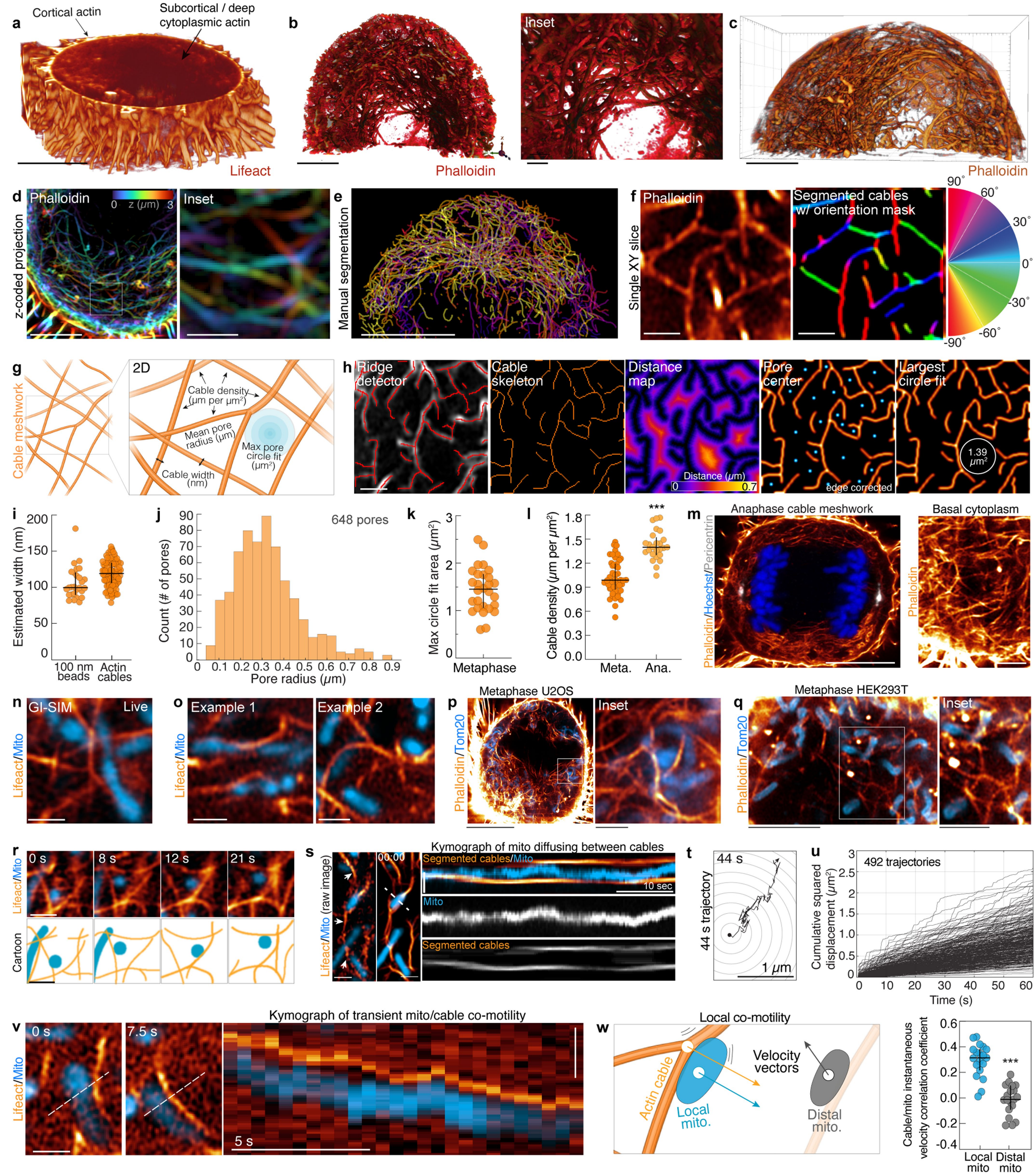

Extended Data Fig. 2 | See next page for caption.

Extended Data Fig. 2 | A 3D meshwork of actin cables associates with mitochondrial networks in the deep metaphase cytoplasm. **a**, 3D rendering of the bottom third of a live, Lifeact–eGFP-expressing metaphase HeLa imaged by SDCM. The cortical actin signal is well resolved, whereas lower-contrast deep subcortical actin assemblies appear hazy and ill-defined. **b**, Shadow projection of subcortical and cytoplasmic actin in a fixed, phalloidin–AF488-stained HeLa cell. Expanded region shows 3D meshwork of actin cables. Volume was acquired by Airyscan microscopy and the brighter cortical actin signal was computationally masked and removed. **c**, Blend projection of actin cables (AF488–phalloidin) in a metaphase HeLa cell. Volume was acquired by Airyscan and processed as in **b**. **d**, *z*-coded maximum-intensity projection of the actin meshwork (AF488–phalloidin) in a prometaphase HeLa with expanded region. **e**, Manual segmentation of actin cables in one half of a metaphase HeLa cell. **f**, Single-slice, Airyscan image of metaphase actin cables (AF488–phalloidin). Segmented cables are pseudocoloured by relative orientation (−90° to 90°). **g**, Cartoon schematic of actin cable meshwork indicating parameters used for analysis. **h**, Representative actin cable analysis workflow showing ridge detection to identify and skeletonize cables, Euclidean distance mapping to identify pore centres, and largest circle fitting technique to estimate maximum pore size. All analyses were performed on 2D slices in the basal metaphase cytoplasm. **i**, Estimated width of actin cables and 100-nm TetraSpeck beads imaged by GI-SIM. Widths are based on full width at half maximum of Gaussian fits of 1-pixel line scans through individual cables. **j**, Frequency distribution of actin mesh pore radii. **k**, Area of largest actin meshwork fitting circle. **l**, Actin cable density in metaphase or anaphase HeLa cells. **m**, Airyscan image of actin cables (phalloidin), DNA (Hoechst) and centrosomes (anti-pericentrin) in a central slice of an anaphase HeLa cell. A magnified view of actin cables in the basal cytoplasm is shown on the right. **n**, GI-SIM image of mitochondria (mito–dsRed2) co-orientation with actin cables (Lifeact–eGFP). **o**, Airyscan images of mitochondria associated with actin cables in live metaphase HeLa cells. **p**, Mitochondria (anti-TOM20) associated with actin cables (phalloidin) in a metaphase U2OS cell. **q**, Mitochondria (anti-TOM20) associated with actin cables (phalloidin) in a metaphase HEK 293T cell. **r**, Airyscan montage and cartoon of a mitochondrion oscillating between actin cables in the metaphase cytoplasm. **s**, Left, raw Airyscan image of mitochondria (mito–dsRed2) and actin cables (Lifeact–eGFP, arrows) in the deep cytoplasm of a metaphase HeLa cell. Right, segmented, median-time averaged image of the same region used in Fig. 1d. Kymograph indicating an individual mitochondrion oscillating between two neighbouring actin cables. **t**, Representative 44-s trajectory of mitochondria within the actin cable mesh. **u**, Cumulative squared displacement of mitochondria diffusing within the actin cable meshwork. **v**, Montage and kymograph of transient mitochondrial co-motility with a local actin cable. **w**, Cartoon indicating co-motility between a cable and an immediately adjacent (local) mitochondrion. Instantaneous velocity correlation coefficient for actin cables with either local or distal mitochondria. Scale bars: 10 µm (**a**, **c**, **e**, **m**, left, **p**); 5 µm (**b**, **d**, **q**); 1 µm (**b** inset, **d** inset, **f**, **h**, **n**, **o**, **p** inset, **r**, **s**, **t**, **v**); 2.5 µm (**m** right, **q** inset). Sample sizes: 100 cables from 20 cells (**i**); 28 cells (**j**, **k**); 46 metaphase cells, 25 anaphase cells (**l**); 19 cells (**w**). Samples were drawn from at least three independent experiments. Statistical tests: two-tailed unpaired *t*-test $^{***}P < 0.0001$ (**l**, **w**); median ± interquartile range (**i**–**l**, **w**).

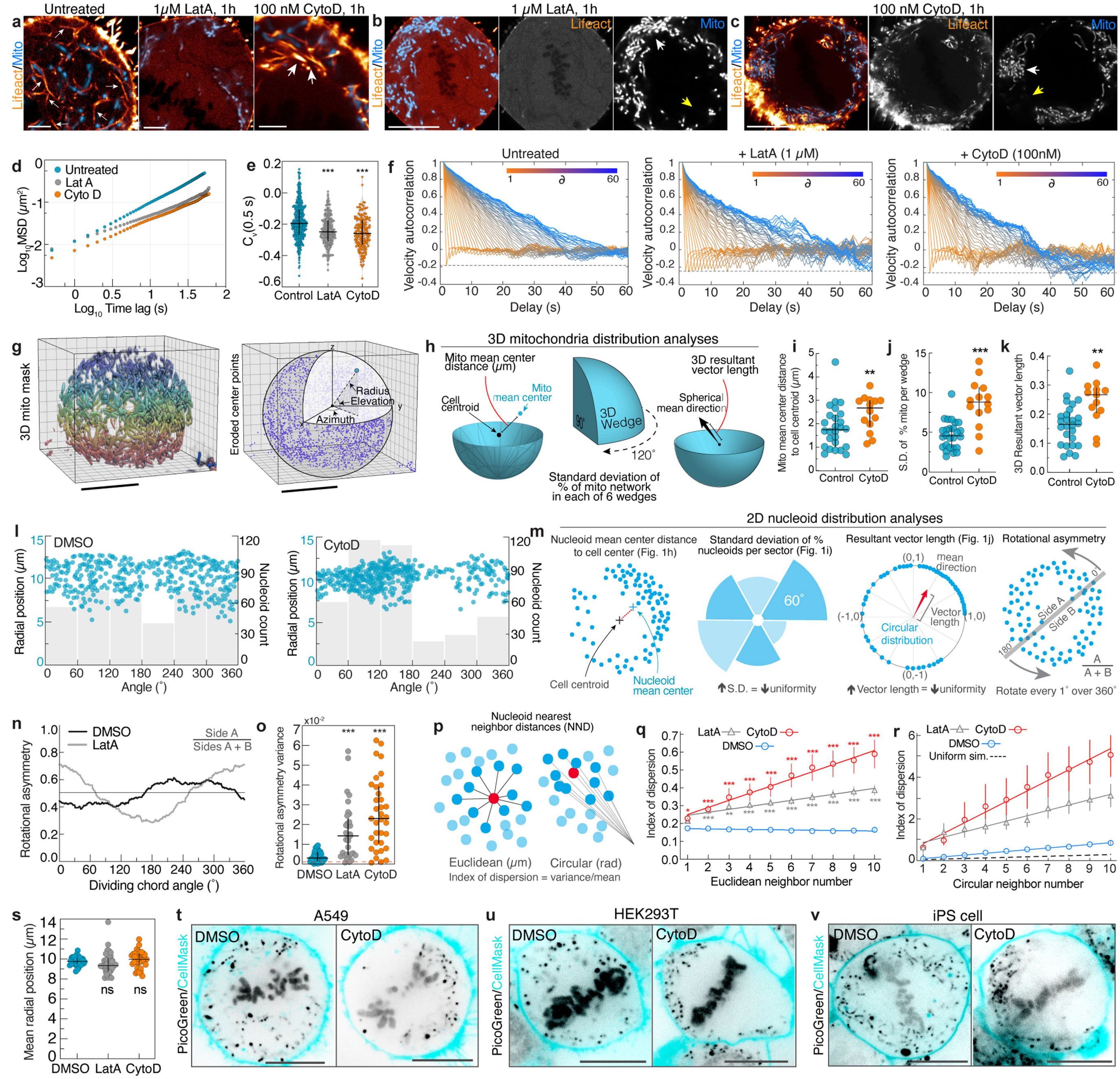

Extended Data Fig. 3 | See next page for caption.

Extended Data Fig. 3 | Disruption of the actin cable meshwork impairs metaphase mitochondrial motility and distribution. a, F-actin (Lifeact–eGFP) and mitochondria (mito–dsRed2) organization in untreated, LatA-treated (1 μM, 1 h) and CytoD-treated (100 nM, 1 h) metaphase HeLa cells. Small arrows indicate actin cable network in untreated cells. Large arrows indicate aggregated actin cables in CytoD-treated cell. **b**, Metaphase HeLa treated with 1 μM LatA for 1 h. LatA treatment eliminated subcortical actin structures (Lifeact–eGFP) with minimal effects on cell geometry. White arrow indicates region of clumped mitochondria (mito–dsRed2). Yellow arrows indicate cytoplasmic regions with decreased mitochondrial density. **c**, Representative metaphase HeLa cells treated with 100 nM CytoD for 1 h. CytoD treatment induced collapse of the meshwork (Lifeact–eGFP) and marked disorganization of actin cables. As with LatA treatment, CytoD treatment induced mitochondrial aggregation (mito–dsRed2). **d**, MSD of 60-s mitochondrial trajectories in untreated, LatA-treated or CytoD-treated metaphase cells. **e**, Velocity autocorrelation at 0.5-s delays ($C_v(0.5\,\mathrm{s})$) for mitochondrial trajectories from untreated, LatA-treated or CytoD-treated metaphase HeLa cells. **f**, Discretized velocity autocorrelations of 60-s mitochondrial trajectories in untreated, CytoD-treated or LatA-treated cells. **g**, Left, 3D segmentation mask of mitochondria (mito–dsRed2) in a live metaphase HeLa cell (pseudocoloured by *z*-position). Right, eroded points derived from the mitochondrial mask with schematic indicating spherical coordinate system with origin at the cell centroid. **h**, Schematic indicating 3D mitochondrial distribution analyses. **i**, 3D mitochondrial mean centre distance to cell centroid in untreated or CytoD-treated cells. **j**, Standard deviation of the percentage of the mitochondrial network in each of 6 equal sized 3D wedges from control (untreated) or CytoD-treated cells. Wedges were specified by azimuthal values of 0°–120°, 120°–240° and 240°–360° in either the bottom hemisphere (that is, elevation −90° to 0°) or the top hemisphere (that is, elevation 0° to 90°). **k**, 3D resultant vector length for control (untreated) or CytoD-treated cells. **l**, Scatter plot of nucleoid radial (*y* axis) and angular (*x* axis) positions superimposed on histograms of nucleoid count per 60° from DMSO- and CytoD-treated cells in Fig. 1g. **m**, Schematic indicating 2D mtDNA nucleoid distribution analyses. **n**, Example rotational asymmetry traces of nucleoids in a DMSO- or LatA-treated metaphase cell. Asymmetry was calculated as the ratio of nucleoids on side A to the total number of nucleoids (sides A + B) upon rotating the dividing chord by 1° intervals over 360°. **o**, Variance of rotational asymmetry over 360° for DMSO-, CytoD- or LatA-treated cells. **p**, Schematic indicating Euclidean and circular nearest-neighbour distance analysis for nucleoids. Index of dispersion for ten nearest neighbours of all nucleoids in a cell is reported. **q**, Index of dispersion of Euclidean nearest-neighbour distances between all nucleoids and their ten nearest neighbours in cells treated with DMSO, LatA or CytoD. **r**, Index of dispersion of circular nearest neighbour distances between all nucleoids and their ten nearest neighbours in cells treated with DMSO, LatA or CytoD. **s**, Mean nucleoid radial position in cells treated with DMSO, CytoD or LatA. **t**, Mitochondrial nucleoids (PicoGreen) and plasma membrane (Cell Mask Orange) in metaphase A549 cells treated with DMSO (left) or 100 nM CytoD (right). **u**, Mitochondrial nucleoids (PicoGreen) and plasma membrane (Cell Mask Orange) in metaphase HEK 293T cells treated with DMSO (left) or 100 nM CytoD (right). **v**, Mitochondrial nucleoids (PicoGreen) and plasma membrane (Cell Mask Orange) in metaphase iPS cells treated with DMSO (left) or 100 nM CytoD (right). Scale bars: 2.5 μm (**a**); 10 μm (**b**, **c**, **g**, **t**–**v**). Sample sizes: 479 control, 232 LatA-treated and 185 CytoD-treated mitochondria trajectories (**d**–**f**); 26 untreated, 14 CytoD-treated cells (**i**–**k**); 36 DMSO-treated, 33 LatA-treated and 35 Cyto-D-treated cells (**o**, **q**–**s**). Samples were drawn from at least three independent experiments. Statistical tests: Kruskal–Wallis test with Dunn's multiple comparisons test ***$P < 0.0001$ (**e**, **o**); two-tailed Mann–Whitney test **$P = 0.0099$ (**i**); two-tailed unpaired *t*-test ***$P < 0.0001$ (**j**); two-tailed unpaired *t*-test **$P = 0.0025$ (**k**); two-way repeated measures ANOVA with Dunnet's multiple comparisons test (**q**), neighbour 1: DMSO vs LatA $P = 0.0833$, DMSO vs CytoD *$P = 0.0288$; neighbour 2: DMSO vs LatA ***$P < 0.0001$, DMSO vs CytoD ***$P = 0.0002$; neighbour 3: DMSO vs LatA ***$P < 0.0001$, DMSO vs CytoD **$P = 0.0026$; neighbour 4: DMSO vs LatA ***$P < 0.0001$, DMSO vs CytoD ***$P = 0.0004$; neighbour 5: DMSO vs LatA ***$P < 0.0001$, DMSO vs CytoD ***$P = 0.0002$; neighbours 6–10: DMSO vs LatA ***$P < 0.0001$, DMSO vs CytoD ***$P < 0.0001$. Kruskal–Wallis test with Dunn's multiple comparisons test (**s**), DMSO vs LatA $P = 0.2294$, DMSO vs CytoD $P = 0.6893$. Median ± interquartile range (**e**, **i**–**k**, **o**, **s**); mean ± s.e.m. (**q**–**r**).

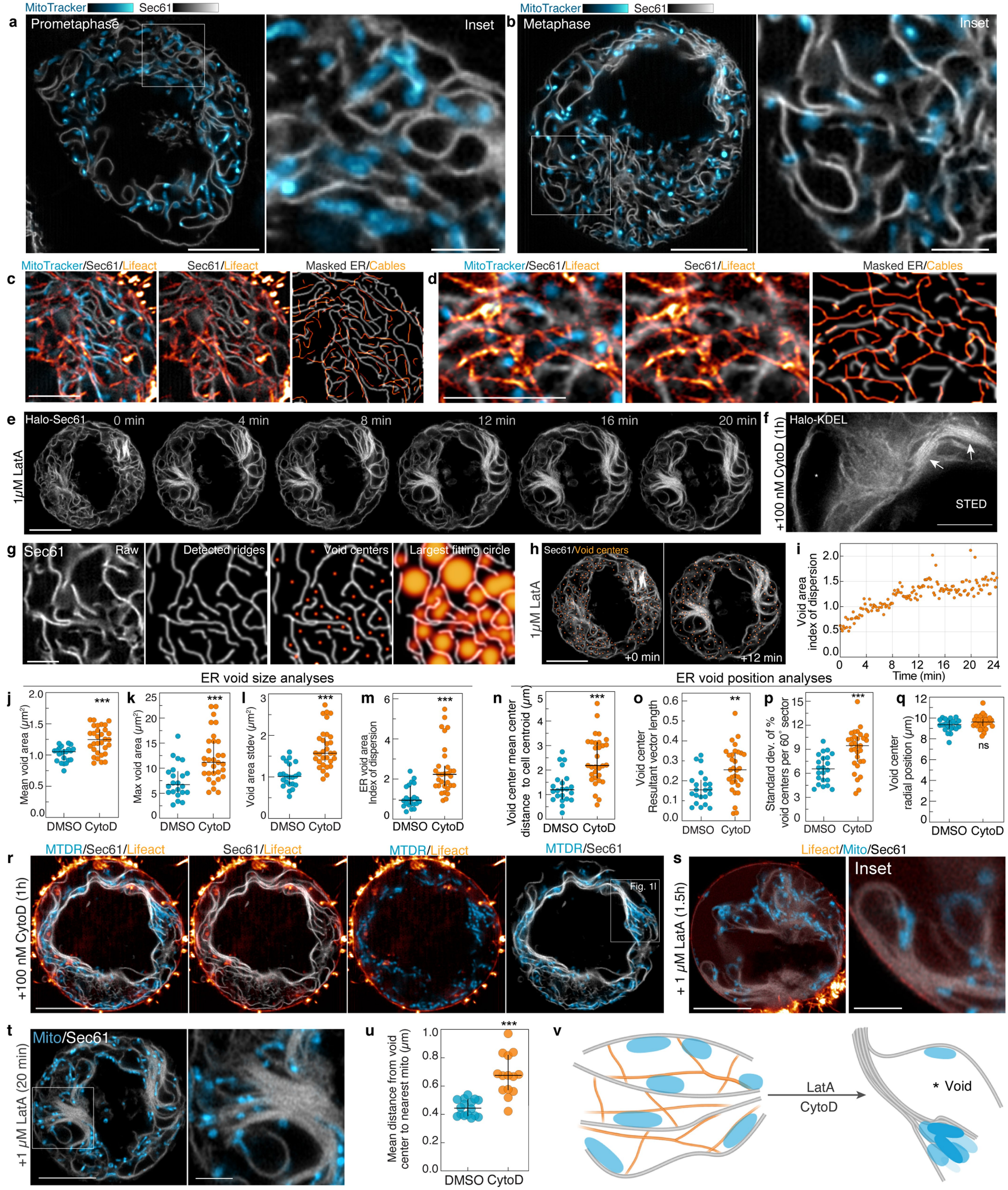

Extended Data Fig. 4 | See next page for caption.

Extended Data Fig. 4 | Disruption of the actin cable meshwork results in metaphase ER collapse. a, iSIM slice of ER (eGFP–Sec61B) and mitochondria (MitoTracker DeepRed) in a prometaphase HeLa. **b**, iSIM slice of ER (eGFP–Sec61B) and mitochondria (MitoTracker DeepRed) in a metaphase HeLa. **c**, iSIM image of ER (eGFP–Sec61B), mitochondria (MitoTracker DeepRed) and actin (Lifeact–mScarlet) with accompanying segmented and masked images. **d**, Airyscan image of mito–dsRed2 (blue), Halo–Sec61B (grey) and Lifeact–eGFP (orange) in a metaphase HeLa cell with accompanying masked images of actin cables and ER profiles. **e**, Airyscan montage of ER cisternal collapse after addition of 1 μM LatA. **f**, STED image of ER (Halo–KDEL) in a metaphase HeLa treated with 100 nM CytoD for 1 h. Arrows indicate tightly stacked ER sheets. Asterisk indicates expanded cytoplasmic void between ER sheets. **g**, Representative analysis workflow for estimating the size of voids between ER sheets. **h**, Time points at 0 and 12 min from **e** are shown with void centre positions in orange. **i**, Index of dispersion (variance-to-mean ratio) of areas of cytoplasmic voids from the cell shown in **e** over 24 min. LatA (1 μM) was added at time 0. **j**–**m**, Inter-cisternal ER void size analyses in DMSO- or CytoD-treated cells, including mean inter-cisternal void area (**j**), maximum void area (**k**), standard deviation of void area (**l**) and index of dispersion of void area (**m**). **n**–**q**, Inter-cisternal ER void centre position analyses, including void mean centre distance to cell centroid (**n**), void centre resultant vector length (**o**), s.d. of void centre occupancy per 60° sector (**p**) and void centre radial position (**q**). **r**, iSIM image of Lifeact–mScarlet, eGFP–Sec61B and MTDR in a metaphase HeLa treated with CytoD for 1 h. Magnified inset is shown in Fig. 1l. **s**, Representative example of cisternal collapse and mitochondrial confinement in a metaphase HeLa treated with LatA (1 μM, 1.5 h). **t**, Airyscan image of the cell from **e** at 20 min showing both ER (Halo–Sec61B) and mitochondria (mito–dsRed2). **u**, Mean distance from void centre positions to nearest mitochondria is significantly increased in CytoD-treated cells. **v**, Cartoon indicating close association between mitochondria (blue) and both ER sheets (grey) and actin cables (orange). Elimination of actin cables by LatA or CytoD results in ER disorganization, characterized by inter-cisternal ER void collapse and expansion, effectively displacing mitochondria from regions of the metaphase cytoplasm. Scale bars: 10 μm (**a**, **b**, **e**, **h**, **r**–**t**); 2.5 μm (**a** inset, **b** inset, **g**, **s** inset); 5 μm (**c**, **d**, **f**). Sample sizes: 22 DMSO- and 31 CytoD-treated cells (**j**–**q**); 16 DMSO-treated, 14 CytoD-treated cells (**u**). Samples were drawn from at least three independent experiments. Statistical tests: two-tailed unpaired *t*-test $^{***}P < 0.0001$ (**j**, **l**, **n**); two-tailed unpaired *t*-test $^{***}P = 0.0003$ (**k**); two-tailed Mann–Whitney test $^{***}P < 0.0001$ (**m**, **u**); two-tailed unpaired *t*-test, $^{**}P = 0.0016$ (**o**); two-tailed unpaired *t*-test, $^{***}P = 0.0002$ (**p**); two-tailed unpaired *t*-test, $P = 0.0975$ (**q**). Median ± interquartile range (**j**–**q**, **u**).

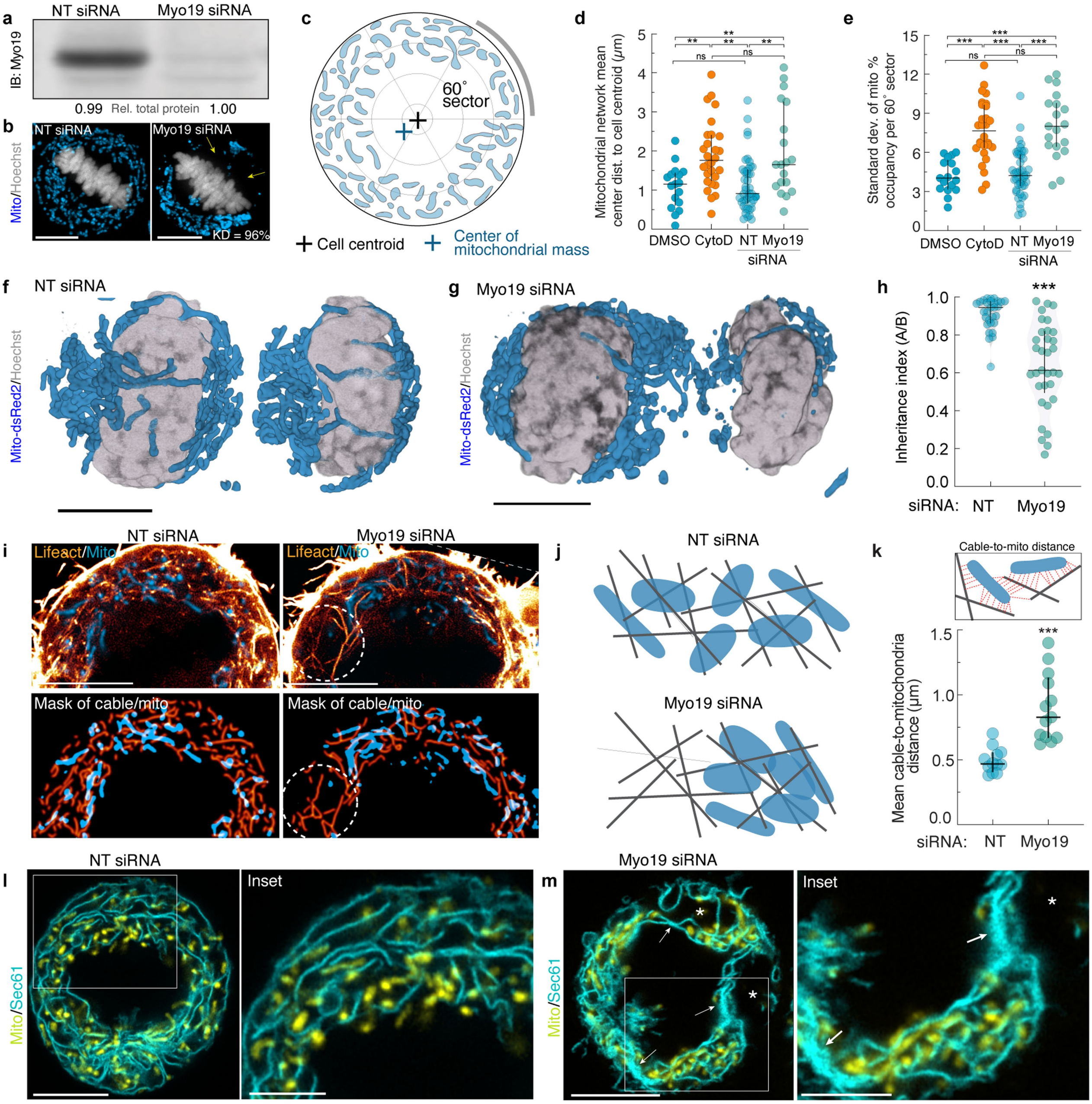

Extended Data Fig. 5 | See next page for caption.

Extended Data Fig. 5 | Myosin19 links mitochondria and associated ER membranes to the actin cable meshwork. **a**, Immunoblot of MYO19 in HeLa cells treated with nontargeting (NT) siRNA or *MYO19* siRNA (right). Relative total protein levels were used as a loading control. Knockdown efficiency was 96%, based on 3 independent experiments. **b**, Spinning disk image of mitochondria (mito–dsRed2) and DNA (Hoechst) in fixed metaphase Hela cells treated with NT or *MYO19* siRNA. Arrows indicate regions of metaphase cytoplasm devoid of mitochondria. **c**, Schematic indicating parameters used for analyses in **d** and **e**, including *xy* centre of mitochondrial mass, *xy* cell centroid, and 60° circle sectors. **d**, Centre of mitochondrial mass displacement from cell centroid in metaphase HeLa cells treated with DMSO (1 h), CytoD (100 nM, 1 h), NT siRNA (40 nM, 48 h) or *MYO19* siRNA (40 nM, 48 h). **e**, Standard deviation of mitochondrial mass per 60° circle sector in metaphase HeLa cells treated with DMSO (1 h), CytoD (100 nM, 1 h), NT siRNA (40 nM, 48 h), or *MYO19* siRNA (40 nM, 48 h). **f**, 3D rendering of mitochondria (mito–dsRed2) and DNA (Hoechst) in cytokinetic HeLa cells treated with NT siRNA. **g**, 3D rendering of mitochondria (mito–dsRed2) and DNA (Hoechst) in cytokinetic HeLa cells treated with *MYO19* siRNA. **h**, Inheritance index (A/B) of mitochondria in cytokinetic HeLa cells treated with either NT or *MYO19* siRNA. Ratio is defined as mitochondrial mass in daughter cell A/mitochondrial mass in daughter cell B, where A is the daughter cell with fewer mitochondria. **i**, Mitochondria (mito–dsRed2) and actin cables (Lifeact-eGFP) in metaphase HeLa cells treated with NT or *MYO19* siRNA. Bottom row, segmented images of mitochondria and actin cables. White circle indicates a region of the cable meshwork largely devoid of mitochondria. **j**, Cartoon of mitochondria and actin cables in the cytoplasm of NT siRNA- or *MYO19* siRNA-treated metaphase cells. **k**, Mean distance (µm) from actin cables to the nearest mitochondrial pixel. Median ± interquartile range. **l**, **m**, Airyscan images of mitochondria (mito–dsRed2) and ER cisternae (Halo–Sec61) in metaphase HeLa cells treated with NT siRNA (**l**) or *MYO19* siRNA (**m**) for 48 h. Arrows indicate collapsed, compacted ER sheets. Asterisks indicate expanded, inter-sheet cytoplasmic voids. Scale bars: 10 µm (**b**, **f**, **g**, **i**, **l**, **m**); 5 µm (**l** inset, **m** inset). Sample sizes: 17 DMSO-, 28 CytoD-, 44 NT siRNA- and 19 *MYO19* siRNA-treated cells (**d**, **e**); 29 NT siRNA-, 33 *MYO19* siRNA-treated cells (**h**); 12 NT siRNA-, 13 *MYO19* siRNA-treated cells (**k**). Samples were drawn from at least three independent experiments. Statistical tests: Ordinary one-way ANOVA with Tukey's multiple comparisons test, DMSO vs CytoD $^{**}P = 0.0087$, CytoD vs NT $^{**}P = 0.0011$, NT vs *MYO19* $^{**}P = 0.0012$, DMSO vs *MYO19* $^{**}P = 0.006$, DMSO vs NT $P = 0.9962$, CytoD vs *MYO19* $P = 0.975$ (**d**); ordinary one-way ANOVA with Tukey's multiple comparisons test $^{****}P < 0.0001$, DMSO vs NT $P = 0.9733$, CytoD vs *MYO19* $P = 0.913$ (**e**); two-tailed Mann–Whitney test $^{***}P < 0.0001$ (**h**); two-tailed unpaired *t*-test $^{***}P < 0.0001$ (**k**). Median ± interquartile range (**d**, **e**, **h**, **k**). An uncropped and unprocessed scan of the blots in **a** is included in the Source Data.

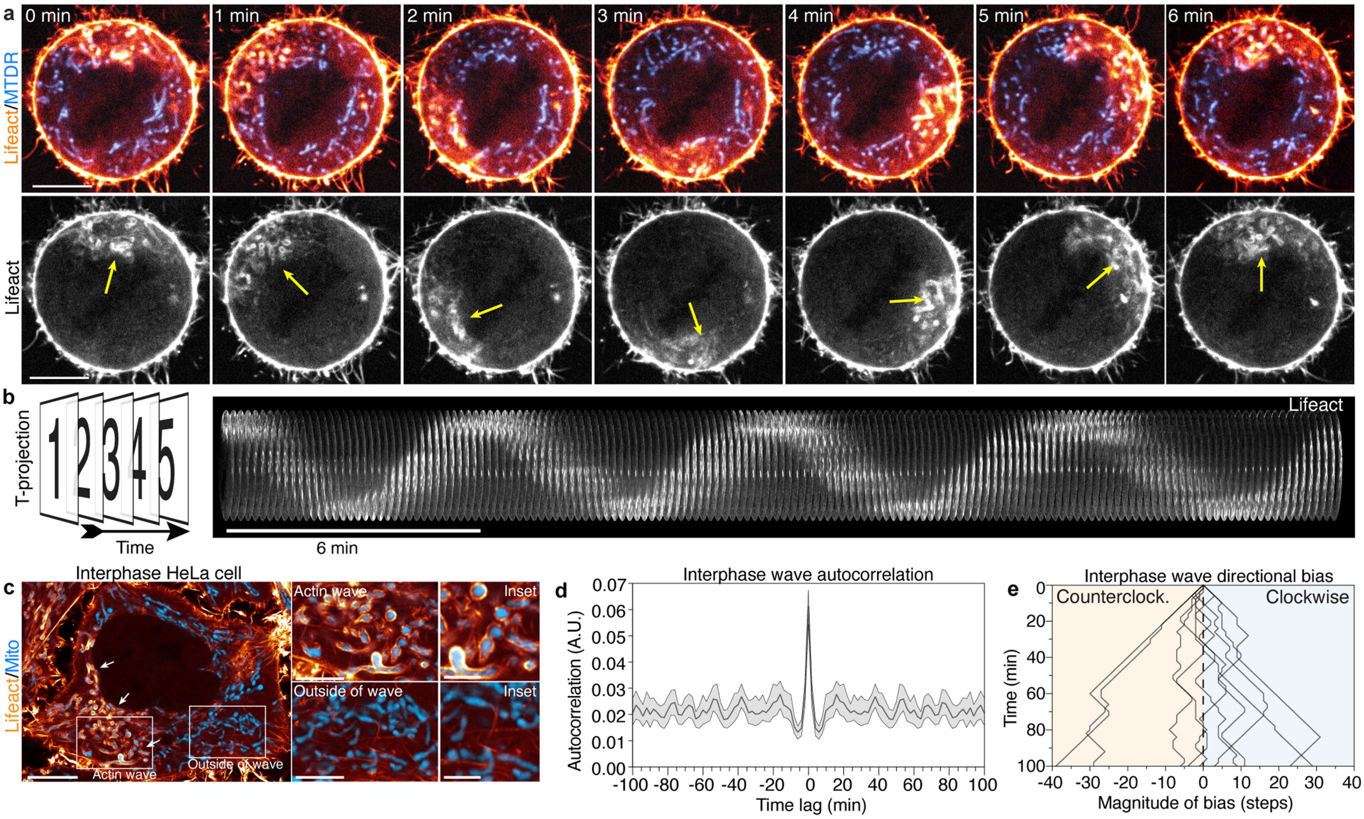

f

Mitotic stage	Wave?
Prophase	20/20
Prometa.	25/25
Metaphase	88/89
Anaphase	20/20
Telophase	13/13

n = 167 cells

g

	Directionality	Period (s)	Probes used to visualize wave	Cell lines with actin waves	Cell lines with no actin waves
Mitochondrial actin wave (this work)	78% uni-directional	382 ± 84	Lifeact^{+++}, Utr-CH^{+++}, F-Tractin^{++}, SiR-Actin^{+}, β-actin^{+}, Phalloidin^{+++}	HeLa, MCF-7, A549, NHEK, COS-7, HaCaT, HEK293T*, MDA-MB-231*, iPS cells*	PTK2, U2OS, RPE1, NIH3T3, bTC3 ARPE19, hippocampal neurons
Actin cluster (Mitsushima et al.)	87% uni-directional	404 ± 117	UtrCH, FP-Actin, Phalloidin, Actin antibody	HeLa, MCF-7, HepG2, Cos1, HaCaT*, HEK293T*, A431*, KB*	NIH3T3, MDCK, C3H10T1/2

Mitochondrial actin labeling quality, $^{+++}$excellent, $^{++}$intermediate, $^{+}$poor

*disorganized waves

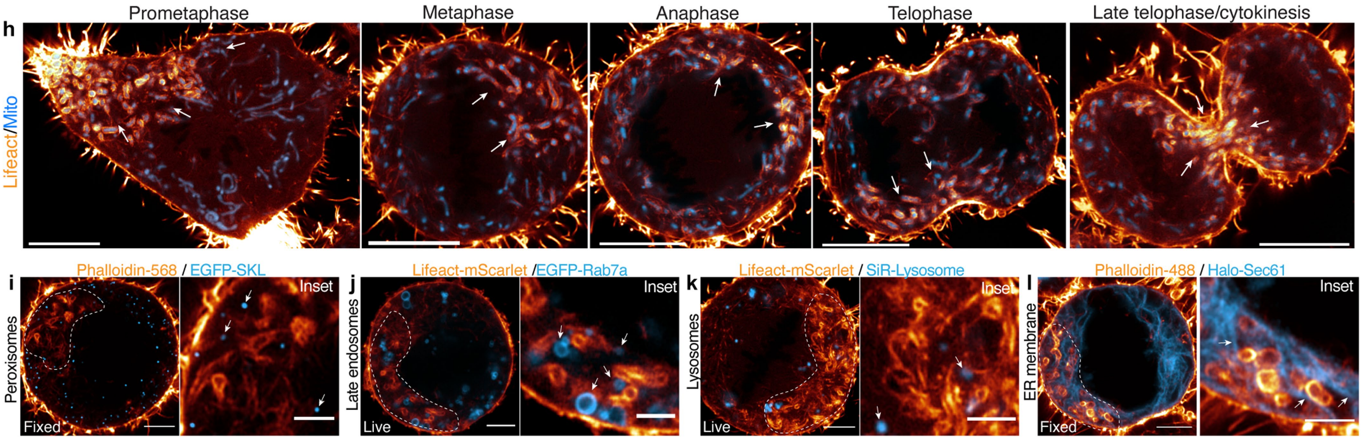

Extended Data Fig. 6 | See next page for caption.

Extended Data Fig. 6 | Mitochondrial actin waves rapidly cycle through mitotic mitochondrial networks. a, Top, spinning disk confocal montage of mitochondria (MitoTrackerDeepRed, MTDR) and F-actin (Lifeact–mScarlet). Bottom, monochrome montage of Lifeact signal with yellow arrow indicating position of the mitochondrial actin wave. Scale bar, 10 μm. **b**, 3D kymograph of metaphase actin wave upon subtraction of cortical actin signal. **c**, Interphase HeLa cell expressing Lifeact–eGFP and mito–dsRed2. Insets indicate mitochondria inside or outside of the actin wave (arrows). **d**, Autocorrelation of interphase actin wave. Mean ± 95% confidence interval. **e**, Directionality of actin waves. Negative values on the *x* axis indicate a net anticlockwise bias after 100 min, while positive values indicate a net clockwise bias. **f**, Fraction of HeLa cells in the indicated stages of mitosis with mitochondrial actin waves. **g**, Table comparing mitochondrial actin waves described here and previously described revolving actin clusters[12]. **h**, Representative images of F-actin (Lifeact–eGFP) and mitochondria (mito–dsRed2) in HeLa cells in different stages of mitosis. White arrows indicate position of the actin wave. **i**, Airyscan image of F-actin (phalloidin) and peroxisomes (eGFP–SKL) in a fixed, metaphase HeLa cell. Dashed line indicates boundary of the actin wave. Arrows indicate peroxisomes outside of actin clouds. **j**, Airyscan images of F-actin (Lifeact) and late endosomes (eGFP–Rab7a) in a live, metaphase HeLa cell. Dashed line indicates boundary of the actin wave. Arrows indicate endosomes outside of actin clouds. **k**, Airyscan images of F-actin (Lifeact) and lysosomes (SiR-lysosome) in a live, metaphase HeLa cell. Dashed line indicates boundary of the actin wave. Arrows indicate lysosomes outside of actin clouds. **l**, Airyscan images of F-actin (phalloidin) and ER (Halo–Sec61) in a fixed, metaphase HeLa cell. Dashed line indicates boundary of the actin wave. Arrows indicate ER outside of actin clouds. Scale bars: 10 μm (**a**, **c**, **h**–**l**); 2.5 μm (**b**, centre, **i**–**l**, insets); 1 μm (**c**, right). Sample sizes: 17 cells (**d**), 10 cells (**e**), 167 cells (**f**). Samples were drawn from at least three independent experiments.

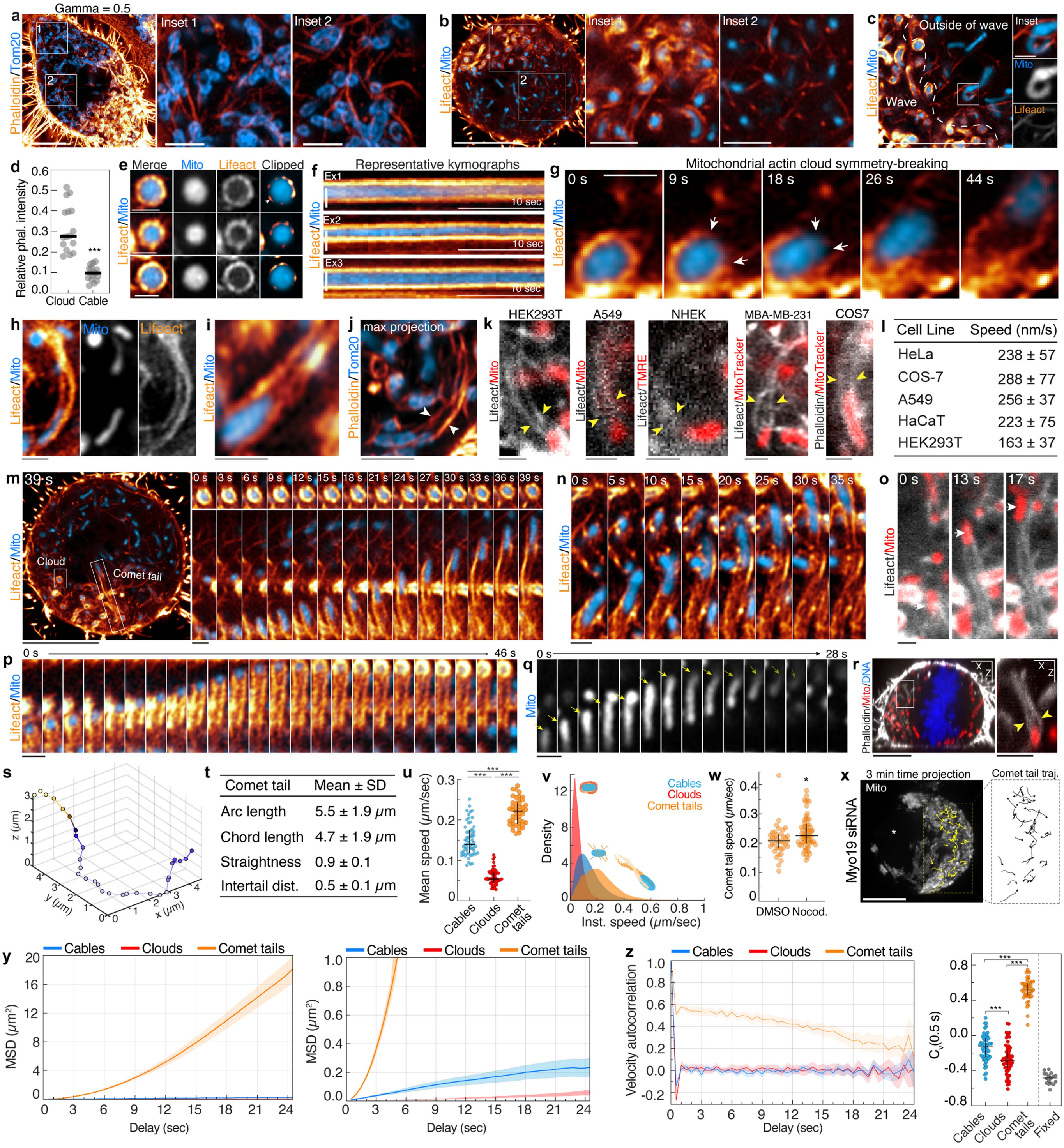

Cell Line	Speed (nm/s)
HeLa	238 ± 57
COS-7	288 ± 77
A549	256 ± 37
HaCaT	223 ± 75
HEK293T	163 ± 37

Comet tail	Mean ± SD
Arc length	5.5 ± 1.9 μm
Chord length	4.7 ± 1.9 μm
Straightness	0.9 ± 0.1
Intertail dist.	0.5 ± 0.1 μm

Extended Data Fig. 7 | See next page for caption.

Extended Data Fig. 7 | Mitochondria associate with actin cables, clouds, and comet tails in mitosis. **a**, Gamma-adjusted version of the image shown in Fig. 2h, revealing lower-intensity actin cables outside of the wave. Insets show mitochondria outside of the wave associated with actin cables. **b**, Live metaphase HeLa cell expressing Lifeact-eGFP and mito–dsRed2 with insets indicating position of actin wave and cables. **c**. Airyscan image of mitochondrial actin clouds within a metaphase actin wave. White dashed line indicates wave border. Expanded regions show mitochondria associated with cables (arrows) outside of the wave. **d**, Relative phalloidin intensity of actin clouds and actin cables. Values represent the ratio of clouds or cables to cortical actin signal. **e**, Representative Airyscan images of mitochondrial actin clouds with clipped images showing bright actin nodes on the surface of mitochondria. **f**, Representative kymographs indicating restricted mitochondrial motility inside of actin clouds. **g**, Airyscan montage of an actin cloud symmetry breaking event. Arrows indicates a gap forming between adjacent nodes in the cloud preceding mitochondrial ejection. **h**, **i**, Representative images of mitochondria associated with actin comet tails in live HeLa cells. **j**. Airyscan maximum-intensity projection of a mitochondrial actin comet tail in a metaphase HeLa. **k**, Metaphase mitochondrial actin comet tails from the indicated cell types. Arrows indicate trailing comet tails. **l**, Speed of comet tail-based motility in the indicated cell types. **m**, Airyscan image of actin (Lifeact–eGFP) and mitochondria (mito–dsRed2) in a metaphase HeLa cell. Montage indicates motility of mitochondria associated with a cloud (top) or comet tail (bottom) over 39 s. **n**, Airyscan montage of mitochondrial comet tail extension. **o**, Spinning disk montage of F-actin (Lifeact–eGFP) and mitochondria (mito–dsRed2) upon comet tail assembly and extension. **p**, Montage of actin comet tail regaining symmetry, forming an actin cloud around the immotile mitochondrion. **q**, Montage of a mitochondrion (yellow arrow) undergoing comet tail motility resulting in movement out of the imaging plane. **r**, *xz* projection of F-actin (phalloidin), mitochondria (mito–dsRed2), and DNA (Hoechst) in a fixed, metaphase HeLa cell. Inset indicates a mitochondrion associated with an actin comet tail that is oriented primarily in the axial plane. **s**, 3D trajectory of a comet tail-propelled mitochondrion from a 3D Airyscan-fast video. Trajectory is coloured by time. **t**, Actin comet tail parameters estimated from 3D volumes of fixed, phalloidin stained cells. **u**, Mean speed of mitochondria associated with the indicated actin structures over 25 s. **v**, Density estimation of instantaneous speeds of cable, cloud and comet tail associated mitochondria. **w**, Speed of comet tails in metaphase HeLa treated with DMSO or 25 µM nocodazole. **x**, Three-minute time projection of mitochondria (mito–dsRed2) in a *MYO19* siRNA-treated metaphase HeLa cell. Comet tail trajectories are shown in yellow and in the expanded inset. Asterisk indicates regions of cytoplasm unexplored by mitochondria over 3 min. **y**, MSD of cable-, cloud- and comet-associated mitochondria. MSD plot with cropped *y* axis is shown on the right to visualize the reduced cable and cloud motility. **z**, Velocity autocorrelations of the three types of motility. $C_v(0.5\,\mathrm{s})$ values are plotted for mitochondria associated with cables, clouds, comet tails, as well as mitochondria in fixed cells to estimate tracking error. Scale bars: 10 µm (**a**–**c**, **m**, **r**, **x**); 2.5 µm (**a**, insets, **b**, insets, **r**, inset); 1 µm (**c**, inset, **e**–**k**, **m**, right, **n**–**q**). Sample size: 16 cells (**d**); 233 HeLa, 40 Cos7, 35 A549, 30 HaCaT, 74 HEK 293T (**l**); 59 cables, 59 clouds, 47 comets (**u**, **v**); 38 DMSO, 61 nocodazole-treated cells (**w**). 57 cables, 47 comets and 59 clouds (**y**, **z**). Samples were drawn from at least three independent experiments. Statistics: two-tailed unpaired *t*-test $^{***}P < 0.0001$ (**d**); Kruskal–Wallis test with Dunn's multiple comparisons test $^{***}P < 0.0001$ (**u**); two-tailed Mann–Whitney test $^{*}P = 0.011$ (**w**); ordinary one-way ANOVA with Tukey's multiple comparisons test $^{***}P < 0.0001$ (**z**). Median (**d**); mean ± s.d. (**l**, **t**); median ± interquartile range (**u**, **w**, **z**, right); mean ± 95% confidence interval (**y**, **z**, left).

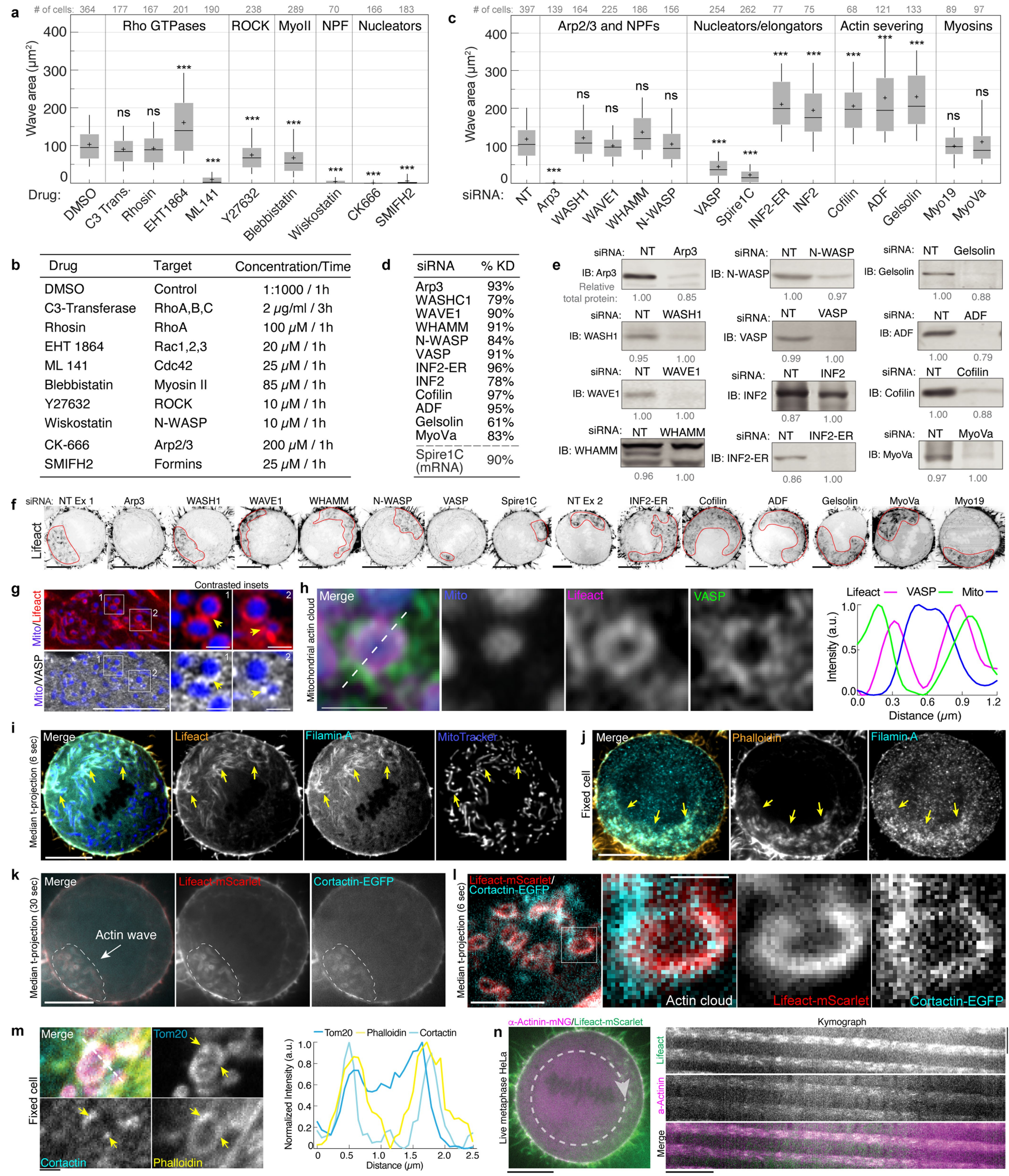

Drug	Target	Concentration/Time
DMSO	Control	1:1000 / 1h
C3-Transferase	RhoA,B,C	2 μg/ml / 3h
Rhosin	RhoA	100 μM / 1h
EHT 1864	Rac1,2,3	20 μM / 1h
ML 141	Cdc42	25 μM / 1h
Blebbistatin	Myosin II	85 μM / 1h
Y27632	ROCK	10 μM / 1h
Wiskostatin	N-WASP	10 μM / 1h
CK-666	Arp2/3	200 μM / 1h
SMIFH2	Formins	25 μM / 1h

siRNA	% KD
Arp3	93%
WASHC1	79%
WAVE1	90%
WHAMM	91%
N-WASP	84%
VASP	91%
INF2-ER	96%
INF2	78%
Cofilin	97%
ADF	95%
Gelsolin	61%
MyoVa	83%
Spire1C (mRNA)	90%

Extended Data Fig. 8 | See next page for caption.

Extended Data Fig. 8 | Mitochondrial actin waves are maintained by multiple actin assembly and disassembly factors. a, Mitochondrial actin wave area in cells treated with indicated inhibitors. **b**, Table indicating the drugs used in **a**, as well as their major targets and concentrations and incubation times used. **c**, Mitochondrial actin wave area in cells treated with indicated siRNA for 48 h. **d**, Knockdown efficiency of siRNAs used in **c**. Values indicate averages of at least three independents experiments. **e**, Representative western blots indicating knockdown efficiency of siRNAs in **c**. Full blots are shown in Supplementary Fig. 1. Relative total protein levels are indicated below each blot. **f**, Representative single-plane images of actin waves (Lifeact–eGFP) in metaphase HeLa cells treated with the indicated siRNAs. Dashed red line indicates wave boundaries. **g**, Airyscan single plane image of a HeLa cell expressing eGFP–VASP (white), Lifeact–mScarlet, (red) and Mito–TagBFP2 (blue). Yellow arrows indicate position of VASP puncta on the actin cloud. **h**, Airyscan image of VASP association with a mitochondrion (Mito–TagBFP2) within an actin cloud (Lifeact–mScarlet). Right, normalized fluorescence intensity of Mito, VASP and Lifeact along the 1-pixel linescan indicated by the dashed line. **i**, Metaphase HeLa cells expressing Lifeact–mScarlet, filamin A–eGFP and MitoTracker DeepRed. **j**, Fixed, anaphase HeLa cell stained for filamin A (cyan) and F-actin (phalloidin, orange). **k**, Spinning disk confocal median time projection (over 30 s) indicating cortactin–eGFP colocalization with Lifeact–mScarlet in a metaphase actin wave. **l**, Median intensity time projection of Lifeact–mScarlet and cortactin–eGFP colocalization in an actin cloud in a metaphase HeLa cell. **m**, SDCM images of fixed HeLa cells stained for mitochondria (anti-TOM20), cortactin (anti-cortactin) and F-actin (phalloidin). White arrows indicate asymmetric, punctate localization of cortactin around actin-positive mitochondria. Right, normalized fluorescence intensity of F-actin (phalloidin), TOM20 and cortactin along the 1-pixel-wide line scan. **n**, Colocalization of α-actinin (α-actinin–mNeonGreen) and F-actin (Life act–mScarlet) in a metaphase HeLa cell. Right, kymograph of LifeAct and α-actinin generated from the indicated line scan (dashed line). Scale bars: 10 µm (**f**, **i**–**k**, **n**); 5 µm (**g**, **l**); 1 µm (**e**, **g**, inset, **l**, inset, **m**). Sample sizes: number of cells per condition is indicated above each box plot (**a**, **c**). Samples are drawn from at least three independent experiments. Statistical tests: Kruskal–Wallis test with Dunn's multiple comparisons test ***$P < 0.0001$, DMSO vs C3 Transferase $P = 0.7515$, DMSO vs rhosin $P < 0.9999$ (**a**); Kruskal–Wallis test with Dunn's multiple comparisons test ***$P < 0.0001$, NT vs *WASH1* $P > 0.9999$, NT vs *WAVE1* $P = 0.6079$, NT vs *WHAMM* $P = 0.0766$, NT vs N-WASP (also known as *WASL*) $P > 0.9999$, NT vs *MYO19* $P > 0.9999$, NT vs *MYO5A* $P > 0.9999$ (**b**). In box plots, centre line shows median, box encompasses the interquartile range, whiskers span 10th to 90th percentiles and '+' indicates the mean. Uncropped and unprocessed scans of the blots are included in the Source Data.

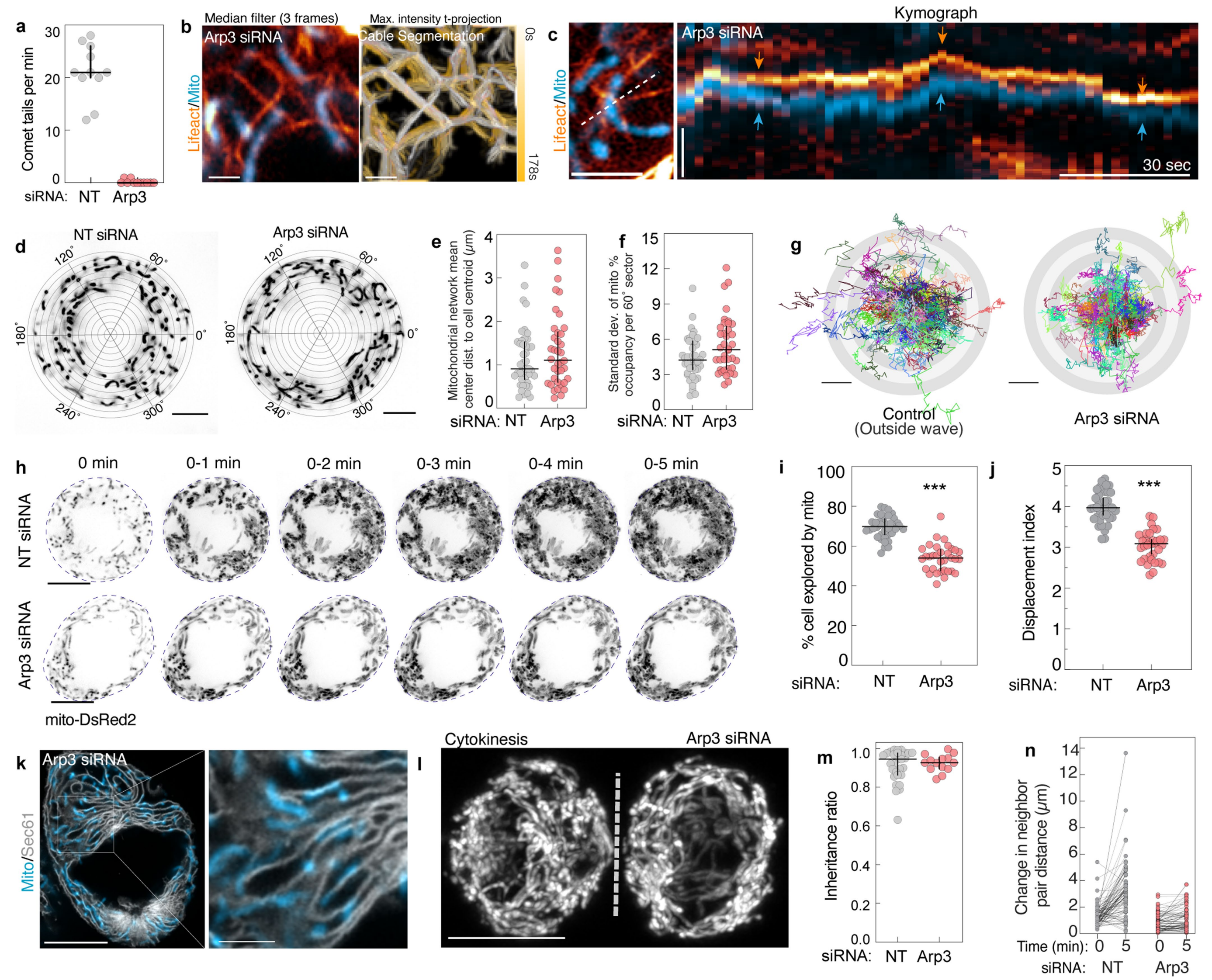

Extended Data Fig. 9 | ARP3 depletion eliminates actin comet tail-based mitochondrial motility but does not impair mitochondrial positioning or equal inheritance. **a**, Frequency of mitochondrial comet tail-based motility over 1 min in metaphase Hela cells treated with NT or *ARP3* siRNA. Median ± interquartile range. $n = 11$ NT siRNA-treated cells, 11 *ARP3* siRNA-treated cells from at least three independent experiments. **b**, Left, three-frame median-intensity time projection of actin cables (Lifeact–eGFP) and mitochondria (mito–dsRed2) in an ARP3-depleted metaphase HeLa cell. Right, time-coded maximum-intensity projection of segmented actin cables over 178 s. **c**, Airyscan image of mitochondria (mito–dsRed2) associated with actin cables (Lifeact–eGFP) in an *ARP3* siRNA-treated metaphase HeLa cell. Kymograph shows mitochondria and cable motility over ~2 min. **d**, Single-plane Airyscan image of mitochondria (mito–dsRed2) in an NT siRNA-treated (left) or *ARP3* siRNA-treated (right) metaphase HeLa cell. **e**, Centre of mitochondrial mass displacement from cell centroid in cells treated with NT or *ARP3* siRNA. Note: the NT data are reproduced from Extended Data Fig. 5e. $n = 44$ NT, 38 *ARP3* from at least three independent experiments. **f**, Standard deviation of mitochondrial per cent occupancy per 60° sector in cells treated with NT or *ARP3* siRNA. **g**, Origin-aligned trajectories for 150 mitochondria over 60 s. Control trajectories were taken from outside of the actin wave in untreated cells. *ARP3* siRNA trajectories are taken from random positions in the cell. **h**, Single-plane cumulative maximum-intensity projections of mitochondria (mito–dsRed2) in NT or *ARP3* siRNA-treated metaphase HeLa cells. **i**, Percentage of cell area covered by mitochondria per min in NT or *ARP3* siRNA-treated metaphase HeLa cells. **j**, Displacement index of mitochondria in NT or *ARP3* siRNA-treated HeLa cells. Displacement index is calculated by dividing mito–dsRed2 area in 5-min maximum intensity time projections by the area of mito–dsRed2 in the first frame. **k**, Mitochondria (mito–dsRed2) and ER (Halo–SEC61) in an *ARP3* siRNA-treated HeLa cell. **l**, Equal mitochondrial inheritance in an *ARP3* siRNA-treated HeLa cell undergoing cytokinesis. Dashed line indicates division plane. **m**, Inheritance ratio (A/B) of metaphase HeLa cells treated with NT or *ARP3* siRNA. Note: NT siRNA data are reproduced from Extended Data Fig. 5. The ratio is defined as mitochondrial mass in daughter cell A/ mitochondrial mass in daughter cell B, where A is the daughter cell with fewer mitochondria. **n**, Change in distance between pairs of neighbouring mitochondria after 5 min in a NT or *ARP3* siRNA-treated metaphase HeLa cell. Scale bars: 1 μm (**b**); 2.5 μm (**c**, **k**, inset); 5 μm (**d**); 500 nm (**g**); 10 μm (**h**, **k**, **l**). Sample sizes: the NT data are reproduced from Extended Data Fig. 5e, 44 NT, 38 *ARP3* siRNA-treated cells from at least three independent experiments (**e**); the NT data are reproduced from Extended Data Fig. 5e, 44 NT, 38 *ARP3* siRNA-treated cells from at least three independent experiments (**f**); 38 NT, 33 *ARP3* siRNA-treated cells (**i**, **j**); 29 NT siRNA, 14 *ARP3* siRNA-treated cells (**m**); change in neighbour distance was calculated on one NT siRNA and one *ARP3* siRNA-treated cell (**n**). Statistical tests: two-tailed unpaired *t*-test, ***$P < 0.0001$ (**i**, **j**). Median ± interquartile range (**a**, **e**, **f**, **i**, **j**, **m**).

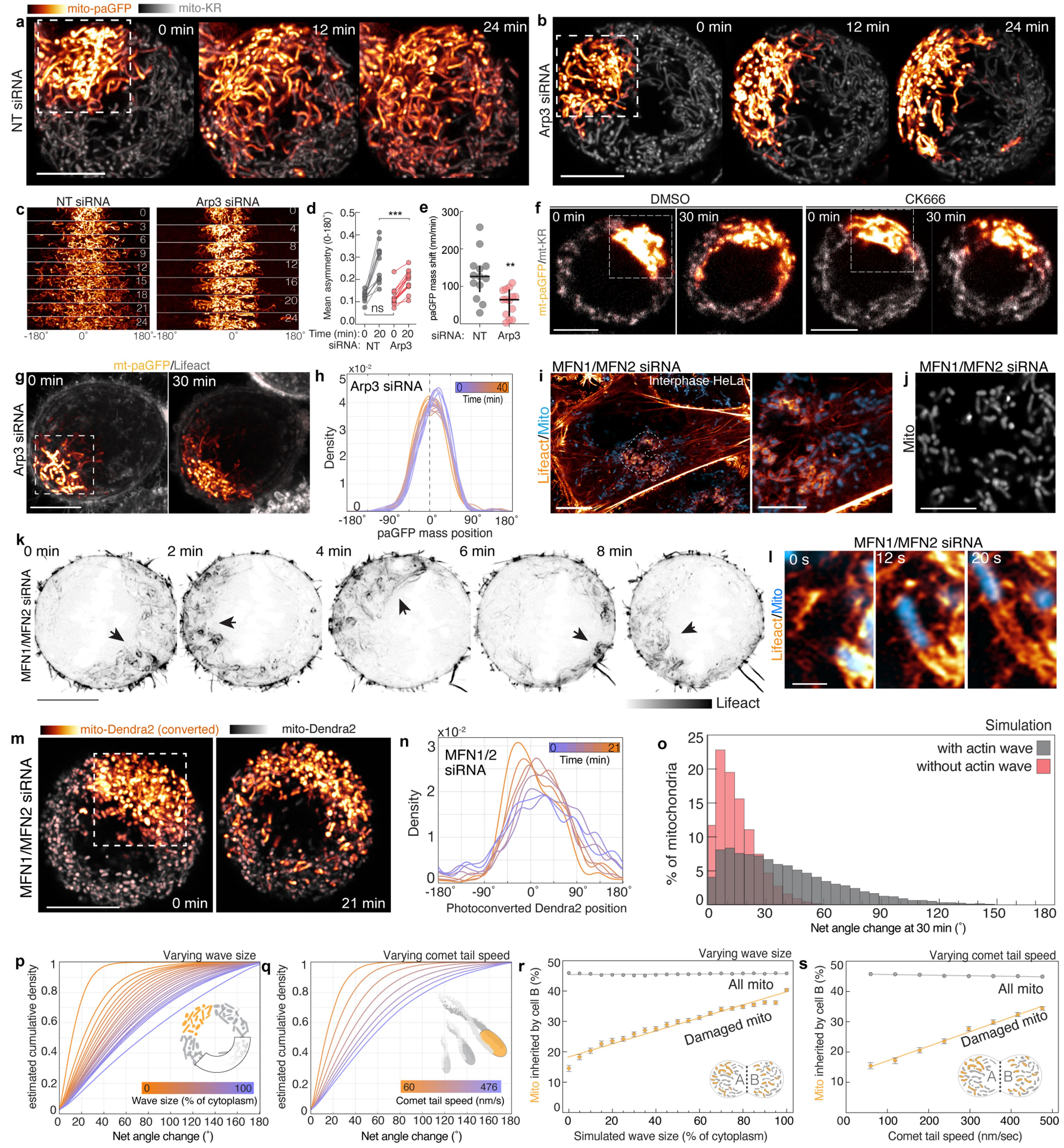

Extended Data Fig. 10 | See next page for caption.

Extended Data Fig. 10 | Actin waves shuffle mitochondrial position before cytokinesis. **a**, **b**, Airyscan maximum-intensity projections of NT siRNA-treated (**a**) or *ARP3* siRNA-treated (**b**) metaphase HeLa cells expressing mito–paGFP and mito–KR. White box indicates region irradiated with 405-nm and 561-nm light to simultaneously bleach Mito–KR and activate mito–paGFP. **c**, Computationally straightened montage of mito–paGFP dispersion in NT or *ARP3* siRNA-treated cells **d**, Mean rotational asymmetry of damaged mitochondria in NT or *ARP3* siRNA-treated cells at 0 and 20 min after photoactivation. **e**, Displacement of damaged, mito–paGFP-labelled mitochondria centre of mass per min in NT or *ARP3* siRNA-treated cells. **f**, Spinning disk maximum-intensity projection of mito–paGFP and mito–KR in metaphase HeLa cells treated with DMSO (left) or CK-666 (right). White boxes indicate regions irradiated with 405-nm and 561-nm light to simultaneously bleach Mito–KR and activate mito–paGFP. **g**, Airyscan maximum-intensity projection of an *ARP3* siRNA-treated metaphase HeLa cell expressing mito–paGFP and Lifeact–mScarlet. White box indicates region irradiated with 405-nm light to activate mito–paGFP. **h**, Circular kernel density estimate of mito–paGFP position over 40 min. Dashed line indicates midpoint of the photoactivation region at time 0. **i**, Airyscan image of *MFN1* and *MFN2* siRNA (MFN1/MFN2)-treated interphase HeLa cell expressing Lifeact–eGFP (orange) and mito–dsRed2 (blue). Dashed line indicates position of the actin wave. Expanded view shows actin-positive mitochondria within the wave. **j**, Airyscan image of fragmented, morphologically simple mitochondria in interphase HeLa cells treated with *MFN1* and *MFN2* siRNA. **k**, Metaphase actin wave (black arrow) persist upon simultaneous depletion of the mitochondrial fusion factors MFN1 and MFN2. **l**, Representative example of actin comet tail-based mitochondrial movements in a metaphase *MFN1* and *MFN2* siRNA-treated HeLa. **m**, Airyscan maximum-intensity projections of a *MFN1* and *MFN2* siRNA-treated metaphase HeLa cell expressing Mito-Dendra2. White box indicates region irradiated with 405-nm light to photoconvert the Dendra2. Over 21 min the photoactivated mitochondria are dispersed through the cell. **n**, Circular kernel density estimates of Mito–Dendra2 distribution over 21 min, indicating increased dispersion of the photoconverted mitochondria over time. **o**, Histogram indicating simulated damaged mitochondrial dispersion over 30 min. Grey boxes indicate net mitochondrial angle change in simulations with actin waves, red boxes indicate net angle change in simulations without waves. **p**, Estimated cumulative density of damaged mitochondria angle change over 30 min in simulations with different sized actin waves. **q**, Estimated cumulative density of damaged mitochondria angle change over 30 min in simulations with different speed actin comet tails. **r**, **s**, Percentage of damaged (orange) and total (grey) mitochondria inherited by daughter cell B over 30 min in simulations with variable wave sizes or actin comet tail speed. Mean ± 95% confidence interval. Scale bars: 10 µm (**a**, **b**, **f**, **g**, **i**, **m**); 5 µm (**i**, inset, **j**); 1 µm (**l**). Sample sizes: 13 NT siRNA-, 14 *ARP3* siRNA-treated cells (**d**, **e**). Samples are drawn from at least three independent experiments. Statistical tests: two-way repeated measures ANOVA with Sidak's multiple comparisons test (**d**), NT vs *ARP3* at 0 min, $P = 0.9927$, NT vs *ARP3* at 20 min, $^{***}P = 0.0006$; two-tailed unpaired *t*-test, $^{**}P = 0.0013$ (**e**). Median ± interquartile range (**e**).

nature research

Corresponding author(s): Erika L.F. Holzbaur

Last updated by author(s): Jan 11, 2021

Reporting Summary

Nature Research wishes to improve the reproducibility of the work that we publish. This form provides structure for consistency and transparency in reporting. For further information on Nature Research policies, see our Editorial Policies and the Editorial Policy Checklist.

Statistics

For all statistical analyses, confirm that the following items are present in the figure legend, table legend, main text, or Methods section.

n/a	Confirmed	
☐	☒	The exact sample size (*n*) for each experimental group/condition, given as a discrete number and unit of measurement
☐	☒	A statement on whether measurements were taken from distinct samples or whether the same sample was measured repeatedly
☐	☒	The statistical test(s) used AND whether they are one- or two-sided *Only common tests should be described solely by name; describe more complex techniques in the Methods section.*
☐	☒	A description of all covariates tested
☐	☒	A description of any assumptions or corrections, such as tests of normality and adjustment for multiple comparisons
☐	☒	A full description of the statistical parameters including central tendency (e.g. means) or other basic estimates (e.g. regression coefficient) AND variation (e.g. standard deviation) or associated estimates of uncertainty (e.g. confidence intervals)
☐	☒	For null hypothesis testing, the test statistic (e.g. *F*, *t*, *r*) with confidence intervals, effect sizes, degrees of freedom and *P* value noted *Give P values as exact values whenever suitable.*
☒	☐	For Bayesian analysis, information on the choice of priors and Markov chain Monte Carlo settings
☒	☐	For hierarchical and complex designs, identification of the appropriate level for tests and full reporting of outcomes
☒	☐	Estimates of effect sizes (e.g. Cohen's *d*, Pearson's *r*), indicating how they were calculated

Our web collection on statistics for biologists contains articles on many of the points above.

Software and code

Policy information about availability of computer code

Data collection	Images were acquired using: Volocity v.6.4 (PerkinElmer), NIS Elements AR v.4.40.00 , Zen Black v.14.0.0.201 (Zeiss), Metamorph v.7.10.1.161, Leica LAS X v.3.1.5.16308 (Leica), and LabView. Immunoblots were imaged with an Odyssey CLx Infrared Imaging System (LI-COR).
Data analysis	MATLAB (R2020a), Circular Statistics Toolbox v. 1.21.0.0, Fiji v. 2.1.0 (NIH), Trackmate v. 6.0.1, ilastik v. 1.3.0, Prism v. 9.0.0 (GraphPad), Imaris v. 9.5.0 (BitPlane), Excel v. 16.36 (Microsoft), Huygens Professional v. 19.04 (Scientific Volume Imaging), Zen Black v. 14.0.0.201 (Zeiss), Image Studio v. 4.0 (LI-COR)

For manuscripts utilizing custom algorithms or software that are central to the research but not yet described in published literature, software must be made available to editors and reviewers. We strongly encourage code deposition in a community repository (e.g. GitHub). See the Nature Research guidelines for submitting code & software for further information.

Data

Policy information about availability of data

All manuscripts must include a data availability statement. This statement should provide the following information, where applicable:

- Accession codes, unique identifiers, or web links for publicly available datasets
- A list of figures that have associated raw data
- A description of any restrictions on data availability

Source data for Figs. 1-3 and Extended Data Fig. 1-10, including data points, statistical test summaries, and P values are included in the Source Data file.

Field-specific reporting

Please select the one below that is the best fit for your research. If you are not sure, read the appropriate sections before making your selection.

☒ Life sciences ☐ Behavioural & social sciences ☐ Ecological, evolutionary & environmental sciences

For a reference copy of the document with all sections, see nature.com/documents/nr-reporting-summary-flat.pdf

Life sciences study design

All studies must disclose on these points even when the disclosure is negative.

Sample size	No sample size calculations were performed, instead sample sizes were empirically determined based on the experimenter's estimation of variability.
Data exclusions	Individual cells in Extended Data Fig 8a,c were excluded from analyses only if they were determined to be unambiguously unhealthy/dying or observed to be in the incorrect stage of mitosis for the given analysis.
Replication	All experimental findings were replicated over at least 3 independent experiments using multiple cell lines and labeling strategies. All attempts at replication were successful.
Randomization	All experimental and control experiments were performed in parallel on otherwise identically treated cells.
Blinding	Investigators were not blinded to group allocation during data collection or analysis. However, mitochondria tracking was performed using a largely automated procedure with minimal manual correction of spurious localizations. Additionally, analyses of mitochondrial nucleoid and ER void positioning was carried out using an automated batch pipeline to minimize bias.

Reporting for specific materials, systems and methods

We require information from authors about some types of materials, experimental systems and methods used in many studies. Here, indicate whether each material, system or method listed is relevant to your study. If you are not sure if a list item applies to your research, read the appropriate section before selecting a response.

Materials & experimental systems

n/a	Involved in the study	
☐	☒	Antibodies
☐	☒	Eukaryotic cell lines
☒	☐	Palaeontology and archaeology
☒	☐	Animals and other organisms
☒	☐	Human research participants
☒	☐	Clinical data
☒	☐	Dual use research of concern

Methods

n/a	Involved in the study	
☒	☐	ChIP-seq
☒	☐	Flow cytometry
☒	☐	MRI-based neuroimaging

Antibodies

Antibodies used	1˚ antibodies: anti-alpha-tubulin clone DM1A (Sigma, T6199, 1:200), anti-Tomm20 (Abcam, ab78547, 1:1000), anti-Tomm20 F-10 (SantaCruz, sc-17764, 1:50), anti-HSP60 LK1 (SantaCruz, sc-59567, 1:100), anti-Filamin 1 E-3 (SantaCruz, sc17749, 1:100), Anti-Arp3 (Proteintech, 13822-1-AP, 1:1000), anti-Cofilin E-8 (SantaCruz, sc-376476, 1:1000), Anti-Gelsolin GS-2C4 (Abcam, ab11081, 1:1000), anti-ADF EPR15827(B) (Abcam, ab186754, 1:1000), anti-Cortactin 4F11 (Millipore, 05-180, 1:100), Anti-pericentrin (Biolegend, 923701, 1:100), Anti-INF2-CAAX and pan-INF2 (gifts from H.Higgs, 1:1000), Anti-N-WASP 30D10 (CST, 4848T, 1:1000), Anti-VASP (CST, 3112, 1:1000), anti-WASHC1 (Atlas, HPA002689, 1:1000), Anti-WAVE1 E2(SantaCruz, sc-271507, 1:200), Anti-WHAMM (Abcam, ab122572, 1:250), Anti-Myosin19 EPR12551-13 (Abcam, ab174286, 1:2000), Anti-MyoVa G-4 (SantaCruz, sc-365986, 1:500). 2˚ antibodies: Goat-anti-rabbit Alexa Fluor 555 (Invitrogen, A-21429, 1:200), donkey-anti-rabbit AlexaFluor 594 (Invitrogen, R37119, 1:1000), Donkey-anti-Rabbit Alexa Fluor 647 (Invitrogen, R37119, 1:1000), Goat anti-Mouse Alexa Fluor 488 (Invitrogen, A-11001, 1:1000), Goat-anti-mouse Alexa Fluor 594 (Invitrogen, A11032, 1:1000), Goat-anti-mouse, Alexa Fluor 647 (Invitrogen, A32728 1:1000), IRDye 800CW Donkey anti-rabbit (Licor, 926-32213, 1:20000), and IRDye 800CW Donkey anti-mouse (Licor, 926-32212, 1:20000).
Validation	Arp3, Cofilin, Gelsolin, ADF, INF2-CAAX, pan-INF2, N-WASP, VASP, WASHC1, WAVE1, Myo19, MyoVa, and WHAMM antibodies were validated for western blot by siRNA knockdown as noted in Extended Data Figure 9e. Alpha-tubulin, pericentrin, Tomm20, HSP60, Filamin1, and Cortactin antibodies were used for immunocytochemistry and reported by their vendor to have human reactivity. No experimental validation was performed, however all primary antibodies used displayed localization patterns consistent with their known subcellular distributions.

Eukaryotic cell lines

Policy information about cell lines

Cell line source(s)	HaCaT (ATCC), COS-7 (ATCC), ARPE19 (ATCC), HEK293T (ATCC), PTK2 (ATCC), U2OS (ATCC). The following cell lines were from academic and not commercial sources: HeLa-M (A. Peden, Cambridge, UK),RPE1 (Janelia Cell Biology Core), MDA-MB-231 (D. Matus, Stonybrook, NY), A549 (O. Quintero, Richmond,VA), NHEK (Penn SBDRC Core), IPS cells (M. Ward, Bethesda, MD).
Authentication	HeLa-M and HEK293T cells were authenticated by STR profiling using GenePrint 10 (Promega, B9510) at the University of Pennsylvania DNA Sequencing Facility. Other cell lines were not authenticated.
Mycoplasma contamination	HeLa-M and HEK293T cells tested negative for mycoplasma using the MycoAlert detection kit (Longa, LT07). Testing was performed periodically. Other cell lines were not tested for mycoplasma, but no visible contamination was ever observed.
Commonly misidentified lines (See ICLAC register)	No commonly misidentified lines were used in this study.